IEEE Open Journal of
Antennas and Propagation

Received 20 January 2022; revised 27 April 2022; accepted 28 April 2022. Date of publication 8 June 2022; date of current version 17 June 2022.

Digital Object Identifier 10.1109/OJAP.2022.3181326

Directionally Resolved Measurement and Modeling of THz Band Propagation Channels

JORGE GOMEZ-PONCE[1,3] (Graduate Student Member, IEEE), NAVEED A. ABBASI[1] (Member, IEEE), ALAN E. WILLNER[2] (Fellow, IEEE), CHARLIE J. ZHANG[4] (Fellow, IEEE), AND ANDREAS F. MOLISCH[1] (Fellow, IEEE)

(Invited Paper)

[1]Wireless Devices and Systems Group, Ming Hsieh Department of Electrical and Computer Engineering, University of Southern California, Los Angeles, CA 90089, USA

[2]Optical Communications Group, Ming Hsieh Department of Electrical and Computer Engineering, University of Southern California, Los Angeles, CA 90089, USA

[3]ESPOL Polytechnic University, Escuela Superior Politécnica del Litoral, ESPOL, Facultad de Ingeniería en Electricidad y Computación, 09-01-5863 Guayaquil, Ecuador

[4]Samsung Research America, Richardson, TX 75082, USA

CORRESPONDING AUTHOR: A. F. Molisch (e-mail: molisch@usc.edu)

This work was supported in part by the Semiconductor Research Corporation under the JUMP Program; in part by the National Science Foundation; in part by the National Institute of Standards and Technology; in part by the Samsung Research America; and in part by the Foreign Fulbright Ecuador SENESCYT Program.

ABSTRACT Design and performance assessment of THz communications systems, which will form an essential part of 6G, require an understanding of the propagation channels the systems will operate in. This paper presents investigations of the channel characteristics in various scenarios at 145 GHz, which is the band currently envisioned for the first round of deployments. In particular, we review several extensive measurement campaigns performed by the University of Southern California in both outdoor and indoor environments. We present the measurement and evaluation methodology and sample results that illustrate the dominant propagation effects in different environments. We then summarize the parameters of the statistical channel models for path loss, delay dispersion, and angular dispersion. Based on these results, we find that even in NLoS (non-line-of-sight) situations, Gbit/s communications can be sustained over a 100 m distance; that (for an antenna gain of 20 dB), there is considerable delay dispersion, requiring tens of equalizer taps, and that angular dispersion is significant in both LoS and NLoS situations. The channel parameters can be thus used as a basis for system design and evaluation under realistic operating conditions.

INDEX TERMS THz communications, channel sounding, path loss, delay dispersion, horn antenna, equalizer, propagation channel, channel modeling.

I. INTRODUCTION

OVER the course of the past decades, there has been a general trend for wireless communications to move to higher and higher frequency bands. This trend is motivated by three factors: (i) the available *absolute* bandwidth, which determines the feasible data rates, increases with the carrier frequency; (ii) there is much fallow spectrum in higher frequency bands - either it is not assigned at all, or not effectively utilized; (iii) progress in semiconductor technology has made it possible to create transceivers for frequency bands that were previously not accessible with low-cost (CMOS) technology. Thus, cellular communications expanded from 450 MHz (used in 1G), to 900 MHz, 2 GHz, and 3.5 GHz, and - in a major step in 5G - to the 24-90 GHz band. The next generation, 6G, will be marked by the use of even higher frequencies, namely the THz spectrum, in particular 0.1-0.5 THz [1]–[3].[1]

1. This spectrum is sometimes called sub-THz, and the 100-300 GHz band may be called high-mmWave; however for brevity and in line with most papers in this area, we will call it THz spectrum.

The three trends we mentioned above as generally driving the use of higher-frequency bands, are also at work specifically for the THz band: (i) new applications, such as holographic communications or extended reality, may require up to 1 Tbit/s data rate, thus greatly exceeding what can be realized in currently used bands [4], [5]. (ii) actions by frequency regulators in various countries (e.g., MIC in Japan, FCC in the USA, OFCOM in the U.K., and CEPT in Europe) are making large swaths of spectrum in the THz band available for communications applications [6], and (iii) improvements in circuit design and semiconductor technology enable manufacturing of critical RF components, such as phased arrays [7], [8] and power amplifiers [9], [10] with low-cost technology. Consequently, THz communications have become of great interest to the community over the past 10 years [11]–[13] and are anticipated to be a major part of 6G systems.

It is axiomatic that the design and evaluation of new wireless systems requires an understanding of, and models for, the wireless propagation channels those systems are to operate in. The channel determines the fundamental performance limits both for single-user systems (e.g., Shannon capacity [14]) and multi-user systems (multi-access and broadcast capacity) [15]. Furthermore, channel characteristics determine which transceiver structures, modulation methods, and signal processing techniques can be used advantageously [16]. An understanding of channel characteristics, as well as suitable channel models, must be based on (or verified by) measurements. Since the underlying multipath propagation of the propagation processes is frequency dependent, the use of a new frequency band such as the THz band requires new channel measurements and models derived from them.

In this spirit, the WiDeS (Wireless Devices and Systems) group at the University of Southern California (USC), in collaboration with Samsung Research USA and the Optical Communications group at USC has performed, over the past 3 years, a number of extensive measurement campaigns in three types of environments and configurations: indoor, outdoor microcell, and outdoor device-to-device (D2D). While detailed description and key results were published in a series of research papers [17]–[21], the current paper aims to systematically summarize the results, provide comparisons between channels in different environments, and quantify several channel parameters beyond those provided in the original papers.

A. THZ APPLICATIONS

The extremely high data rates enabled by THz communications enable a variety of applications. One important use case is ultra-high-speed wireless local area networks (WLANs) and personal area networks (PANs), which are generally in indoor, especially residential or office, environments. These networks can be used for holographic communications [5], wireless connections of extended-reality headsets to their associated powerful computation engines [22], information kiosks that allow ultra-fast downloading of large amounts of content [23], and similar applications for office use and entertainment. While current WLAN systems are limited to about 10 Gbit/s (both in the 6 GHz band and the 60 GHz band), THz applications envision between one and two orders of magnitude faster speeds. The typical placement of an access point is near the ceiling, $2-3$ m above the floor.

High-rate communications are also desirable in outdoor scenarios. Be it in a cafe, city square, or sports stadium, applications like extended reality, watching high-resolution replays or holographic re-enactments, and real-time gaming, will create demand for THz communications systems [24]. In addition to the high data rate, these systems will also have a higher density of users, necessitating multi-user MIMO, and making information about angular dispersion particularly relevant [25]. The typical height of base stations (BSs) ranges from $2-4$ m (typical WLAN access point height) to $10-20$ m (a typical microcellular BS height [26]).

Gaming, social networking, and real-time sensing and control for autonomous driving and similar applications, also motivate the use of D2D communications, where two user devices are communicating directly with each other [27]. This not only reduces the strain on the infrastructure nodes, but also reduces the latency - an aspect that is of particular importance in the above-mentioned applications [28]. In D2D settings, both the transmitter and receiver (Tx and Rx) are at the same height, typically between 1 and 1.8 m above the ground. In particular for outdoor environments, the difference in height of such a device compared to a BS is quite significant and leads to fundamentally different propagation channel characteristics.

For both outdoor and indoor applications, research and standardization activities have begun. In particular, for indoor applications, the IEEE 802.15.3d standard has been recently established. It specifies switched point-to-point links, using either single-carrier modulation (using up to 64 QAM) or on-off keying, and operates in the 250-320 GHz band, which can either be used completely, or can be divided into sub-bands [29]. Theoretically, more than 300 Gbit/s can be realized. However, future work will be needed to realize actual practical systems. A number of large-scale research projects have started all over the world to bring THz systems to reality, both in industry, and in academia.

Besides the above-discussed applications, THz communications is also envisioned for a number of other applications, such as backhaul links for cellular applications, connections between servers in data centers, and other high-speed point-to-point links [30]–[32]. THz links are also useful for wireless connections between computer boards, and even between chips on the same board [33]–[35]. Finally, on-body networks, as well as in-body networks and related medical applications are anticipated. Those topics are beyond the scope of the current paper, and we refer to the survey papers [3], [11]–[13] for a description.

B. LITERATURE REVIEW

There have been a number of directional or double-directional (i.e., directionally resolved at one or both link ends, respectively) channel measurements in indoor environments. The earliest we are aware of are from TU Braunschweig, which measured in a variety of indoor environments [36], [37]. The measurements were done with a vector network analyzer (VNA) in a static environment. Emphasis was on the frequency range around 300 GHz, in line with the band for IEEE 802.15.3d devices. Further measurements were done by a variety of research groups, e.g., [38]–[47].

For outdoor measurements, the number of available double-directional measurements is much smaller. As a matter of fact, our measurements in [48], [49] were the first long-distance double-directional measurements. Recently, NYU [50]–[52] presented a measurement campaign and a channel model derived from it; measurements are done in the 140 GHz range, and the BS height is 4 m, i.e., a typical access point height (while our outdoor measurements are with a BS height of 1.6 m for the D2D scenario, and 11 m for the microcell scenario). The measurements of [53] are for a street canyon at 300 GHz.

A variety of channel models has been developed, based on measurements, as well as deterministic simulations ranging from finite-difference time domain to point-cloud-based ray tracing, to simple ray launching. For a comprehensive survey, the reader is referred to [54].

C. STRUCTURE OF PAPER

The remainder of the paper is organized as follows: Section II reviews the fundamental propagation processes and their frequency dependence. This is followed by a description of our measurement setup in Section III. Next, Section IV discusses the condensed channel parameters we analyzed and their impact on system design. The measurement environments are described in Section V. A number of sample impulse responses and angular spectra, and their physical interpretation, in Section VI is followed by the statistics of the channel parameters in the investigated environments in Section VII. Section VIII then analyzes system performance, including the impact of various beamforming strategies, in the measured channels. Conclusions and outlook to future work wraps up the paper.

II. THZ PROPAGATION EFFECTS

In a wireless channel, signals can propagate via different routes from the Tx to the Rx, interacting with objects in the environment along the way. The different signal echoes, or multipath components (MPCs) thus undergo different propagation processes along the way, in particular one or more of the following (i) free-space path loss, (ii) atmospheric attenuation, (iii) specular reflection/transmission, (iv) diffraction, (v) diffuse scattering, and (vi) Doppler shift. In the following we review the frequency dependence of each of those processes, which will help later to interpret the measurement results.

Free-space path loss describes the "thinning out" of the area power density as the distance between Tx and observation point increases. In the far field (beyond the Rayleigh distance), the ratio of receive power to transmit power in free space is [16]

$$\frac{P_{\mathrm{Rx,FS}}}{P_{\mathrm{Tx}}} = G_{\mathrm{Tx}} G_{\mathrm{Rx}} \left(\frac{c_0}{4\pi f d} \right)^2 = A_{\mathrm{Tx}} A_{\mathrm{Rx}} \left(\frac{f}{c_0 d} \right)^2, \quad (1)$$

where c_0 is the speed of light, G_{Tx} and G_{Rx} are the antenna gains at Tx and Rx respectively, A_{Tx} and A_{Rx} are the antenna area at Tx and Rx respectively, f is the considered frequency, and d the distance between Tx and Rx. The term $(\frac{4\pi f d}{c_0})^2$ is known as the free-space path loss. The left equality, also known as Friis' law, is more commonly used and indicates that when the antenna gain is independent of frequency, path gain decreases with the square of the carrier frequency. However, the right equality shows that for constant antenna *area*, the path gain actually increases with the square of the frequency. This is because of the constant form factor (i.e., geometric area), an antenna becomes *electrically* larger, and thus increases gain and reduces beamwidth.

For mobile and nomadic access scenarios, the antennas have to be adaptive arrays that can steer the narrow beam into the correct direction. Thus, array antennas with fixed area have to increase the number of antenna elements with the square of the frequency.

Consequently, when considering possible antenna gain, two limitations need to be considered: (i) limited antenna area due to constraints on the form factor, and (ii) limited gain due to constraints on the number of antenna elements, which arises from cost and energy consumption considerations. In our campaigns, we measured with (horn) antennas with 21 dB gain, which could be achieved by phased arrays with approximately 64 antenna elements (assuming an element gain of 3 dB). Link budgets and achievable distances discussed later assume this value, which might be realistic at least for early deployments of THz systems.

During propagation through the atmosphere, THz radiation can also be absorbed or scattered by oxygen, and water molecules [55], [56]. One of the most challenging atmospheric effects for this band is rain. In [57], [58], a thorough study in the sub-THz band is shown. This study analyzes its behavior concerning rainfall rate; it indicates that the attenuation can reach up to 20dB/km for extreme rain cases. These values are reduced tenfold due to the maximum considered distance ($\approx$ 100)m. For these reasons, in the 140 GHz band, which is the band of interest in this paper, the attenuation due to atmospheric effects is not significant over the measured range.

Many materials used in building construction have high reflection coefficients for THz signals, including glass, steel concrete, and gypsum boards. However, reflection might occur as either specular or diffuse reflection, and the relative

importance of those contributions depends on the smoothness of the surface. Note that the definition of roughness is relative to the wavelength; for THz frequencies, even minor roughnesses (order of mm) have significant impact [59], [60]. The diffuse scattering might be radiated into a continuum of directions; the simplest model is a Lambertian radiator [61], while more involved models may assume "beams" centered on the direction of specular reflection, and possibly the direction of incidence [62]. Transmission loss is generally quite high; even drywall can attenuate the signal by more than 20 dB [63].

It is well known that the effectiveness of diffraction processes decreases with frequency, i.e., objects throw "sharper shadows" at higher frequencies. Thus, while the uniform theory of diffraction [64] provides a good mathematical description of the diffraction coefficient [65] for practical purposes, the diffraction at 140 GHz can be mostly neglected, except for very shallow diffraction angles. For instance, [66]–[68] show diffraction analysis between 73 GHz and 2 THz. In these studies, the attenuation shown can reach up to 40dB, depending on the angle, and the relative gain obtained by diffraction is $\leq 2dB$ in small angles, congruent with our previous statement.

Finally, Doppler spread may be a significant factor in THz systems, due to the fact that Doppler shifts increase linearly with the carrier frequency. Note, however, that beamforming in particular at a moving device reduces the angular range from which signals are incident, and thus reduces the Doppler spread. Consequently, the Doppler spread might increase sublinearly with frequency if the beamwidth changes with frequency, e.g., in a constant-area antenna. Our measurements were done with static Tx and Rx, so that no Doppler shifts occur during the measurements. However, since we measured the angular power spectra at both link ends, a Doppler spectrum can be synthesized from those measurements from the well-known relationship between angular spectrum and Doppler spectrum [69].[2]

III. MEASUREMENT SETUP

Our measurement system is based on a combination of (i) VNA, (ii) frequency-extenders, and (iii) rotating horn antenna, as well as Radio-over-fiber connections to enable large distances between Tx and Rx antennas, see Fig. 1.

At the core of the sounder is a 4-port VNA, model Keysight PNAX N5247A, which covers a frequency range of up to 67 GHz. It is combined with VNA extenders WR-5.1VNAX from Virginia Diodes. These extenders receive an external local oscillator (LO) signal in the range of $11.33 - 18.33$ GHz, and multiply it internally with a multiplication factor 12, and furthermore mix it with an IF signal that is at 279 MHz. We configure the setup such that both the intermediate frequency (IF) and the LO signals are generated by the ports of the VNA, and thus derived from the same precision clock, leading to high phase stability of the setup.

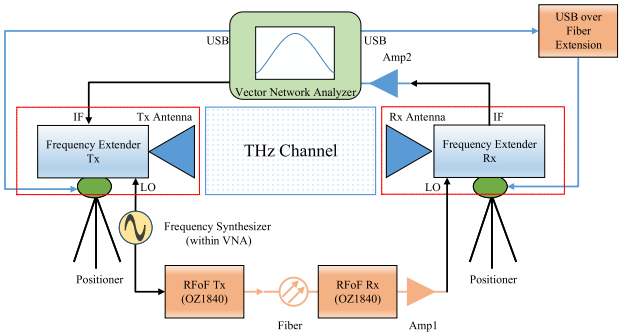

FIGURE 1. Block diagram of the measurement setup.

The transmit power of the frequency extender is -1 dBm where, as discussed in the previous section, the horn antennas for the Tx and Rx provide a gain of 21 dB. For an IF bandwidth (IFBW) of 10 Hz, the system's dynamic range is nearly 120 dB. The Rx frequency extender uses a high-sensitivity waveguide that enhances this dynamic range by a further 20 dB. The dynamic range of the setup can be adjusted by the choice of the IFBW, trading off measurement sensitivity with measurement duration. In most of our measurements, 1 kHz was chosen as IFBW. For outdoor measurements, we use frequency steps of 1 MHz spacing for the VNA, leading to a maximum resolvable excess run-length of 300 m, which is sufficient for all the scenarios we investigated - while longer-delayed MPCs might exist, their power is too low to play a significant role. For indoor, we use stepwidth of 625 kHz, in order to retain comparability to our existing indoor measurements at lower frequencies. We measure over a 1 GHz bandwidth; while larger bandwidths might be of interest for THz systems, the time required for a frequency sweep is linearly proportional to the bandwidth, and larger bandwidths would have increased the total measurement time (see below) beyond the feasibility limits.

The feasible distance from the VNA to the Tx and Rx antennas in measurements from the literature is limited by the cable losses at the LO frequency (in our case at nearly 12 GHz), resulting in maximum measurement range of around 10 m.[3] To circumvent this problem, we introduced in [48] a radio-over-fiber (RoF) setup that modulates the LO signal to the optical domain, where it is transported by a low-loss fiber, and downconverted at the LO port of the remote antenna. While our earliest measurements [48] were done with an RoF setup that was created from available discrete components, our later measurements [17], [18], [20], [21] used a more robust commercial RoF setup (Optical Zonu OZ1840). Fig. 2 shows a comparison of measurements made with the RoF connection compared to a conventional

2. Note that this requires that the beamwidth of the analyzed device is significantly larger than the beamwidth of the antenna in our measurement system.

3. We assume here that the frequency extenders are co-located with the antennas, so that only the LO signal must be transmitted to the remote location. Transmission of the actual THz RF signal would be affected by even higher losses.

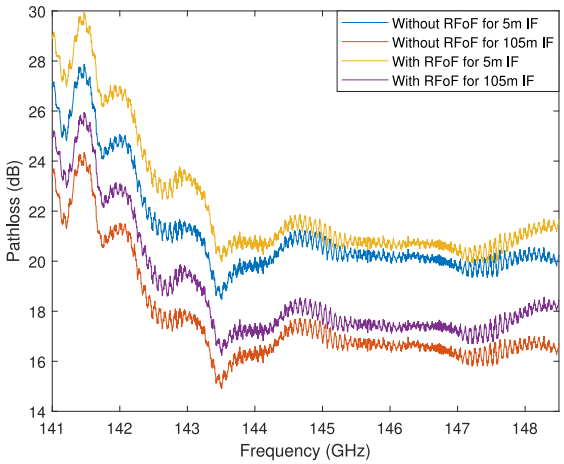

FIGURE 2. Comparison of measurement with and without the RoF extension in an indoor environment for a channel length of 2.4 m.

cable connection.[4] We see that the shapes of the measured path loss curves agree, and a suitable calibration can account for the attenuation difference related to the RoF and the IF cable [48].

The directional characteristics were measured by mechanically rotating horn antennas to cover the desired range in azimuth and elevation. Our horns have a beamwidth (full width half maximum, FWHM) of 13°. In azimuth the antennas were rotated in steps of 10° for all our measurement cases, though the range over which rotation occurred varied from cases to case, see below.

By definition, 0° azimuth corresponds to the case where both the Tx and Rx are facing each other - this is the definition irrespective of whether the optical LoS is obstructed or not.[5] To maintain a uniform definition of elevation in all measurement campaigns regarding the elevation, we define the "co-elevation" as the "initial elevation" orientation (i.e., offset) from which the measurement is performed. This offset depends on the specific campaign. For D2D measurements, both Tx and Rx were always oriented in the horizontal plane (co-elevation $\tilde{\theta} = 0°$) and the azimuth range for both Tx and Rx is $[0°, 360°]$. For the microcellular measurements, the co-elevation was defined such that the geometrical connection between Tx and Rx was $\tilde{\theta} = 0°$, irrespective of whether a line of sight existed or not. We performed measurements with both Tx and Rx in positions $\tilde{\theta} = 0°, \pm 13°$, leading to a total of 9 elevation combinations. The azimuth rotation range for the Tx covered a 120° sector from $[-60°, 60°]$ while the Rx scanned the entire azimuth range $[0°, 360°]$. For the indoor measurements, co-elevation is defined with respect to the horizontal plane, and we performed elevation scans for $\tilde{\theta} = 0°, -10°, -20°$ on the Tx since the Tx is already almost at ceiling height and looking up does not provide significant information (more in Section V) whereas at the Rx we have three elevations with $\tilde{\theta} = 0°, \pm -10°$. Overall, the indoor measurements also result in 9 elevation combinations, just like the microcellular measurements. The azimuth scan resolutions for the indoor measurements are similar to the microcellular measurements.

The reason for choosing 13° resolution in elevation for the microcellular is that the spacing is equal to the FWHM beamwidth, and thus the addition of the elevation measurements results in an effective antenna pattern that is uniform over the range they are combined, collecting all the multipath energy over all (practically relevant) elevation angles.[6] For microcellular measurements the range is $[-13°, 13°]$ the effective FWHM beamwidth is 39 degrees, whereas, for the indoor measurements, the range is $[0°, 20°]$ at the Tx and $[-10°, 10°]$ on the Rx resulting in an effective FWHM beamwidth of 33 degrees (with some overlap in beams) on both sides.

The measurement setup was calibrated at the beginning of each measurement day, to account for possible changes of the electronic components. Due to the use of the high-sensitivity waveguide, a true "back-to-back" calibration, where Tx and Rx are connected via cable, is not permissible (would overload and damage the Rx). Therefore, "over-the-air" (OTA) calibration was performed, with Tx and Rx antennas aligned along LoS direction over a short distance. For the indoor and D2D measurements, this distance was chosen to be between 0.5 m and 2.5 m (ensuring antenna far field), while for the microcellular measurements, it was larger (between 20 and 40 m), due to the significant height difference between Tx and Rx (and the resulting impossibility of placing the Rx in closer proximity to the Tx without disconnecting the cables and thus destroying the calibration). Delay filtering was used in either case to eliminate residual MPCs. We apply the CLEAN algorithm [70] in the inverse Fourier transform of the OTA calibration with a narrow delay window centered in the delay bin corresponding to the LOS. Applying this strategy, we eliminate long delay bins in the calibration that do not constitute the system's response but rather multipath. An example of this procedure is shown in Fig. 3.

Besides measurements with a VNA-based setup, other arrangements using pn-sequences, chirps, or multi-carrier signals as sounding signals are possible for THz channel sounding [71]. We chose the VNA setup both because of its flexibility and the high phase stability that can be used for high-resolution parameter estimation. The two main drawbacks of the VNA setup are the long measurement time, and the need for a cable/fiber connection between Tx and Rx. The former issue is of limited concern as long as the measurement duration is dominated by the mechanical rotation time. The latter issue is overcome by measuring in locations that stay under our control (e.g., campus) for the duration of

4. To enable measurement with the conventional connection, the distance from Tx to Rx was kept to 2.4 m; however, the optical fiber between VNA and Rx still had a length of 105 m also in this case.

5. Deviations from this convention for indoor corridor measurements will be discussed separately in Section VI.

6. The motivation for using 10° in indoor measurements spacing stems from retaining comparability to our earlier 5GHz measurements in the same environment. The non-uniformity introduced by this revised spacing into the effective antenna pattern is less than 2 dB.

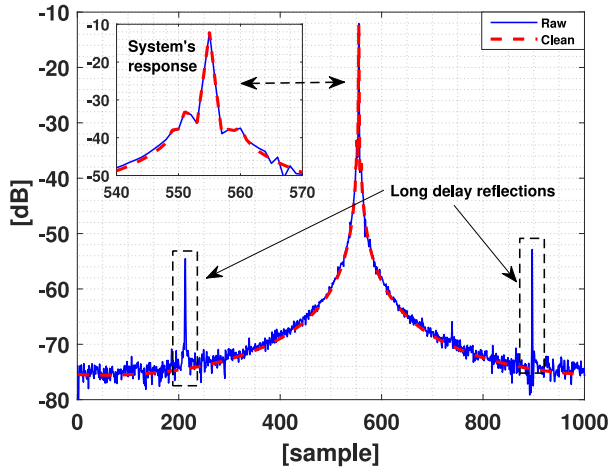

FIGURE 3. Delay filtering process in sample OTA calibration.

the measurement, and a suitable "over-the-air" calibration, as described above. Note that due to the long measurement time of a mechanically rotating horn, the environment needs to remain quasi-static over several hours (i.e., absence of pedestrians and vehicles), and thus has to be under control of the experimenters.

IV. PARAMETERS AND THEIR SYSTEM IMPACT

For each pair of horn orientations $(\phi_{\mathrm{Tx,i}}, \theta_{\mathrm{Tx,j}})$, $(\phi_{\mathrm{Rx,k}}, \theta_{\mathrm{Rx,l}})$ the measurement setup provides a transfer function $H_{\mathrm{meas}}(f)$ at the discrete frequency points f_n through which the VNA steps. The transfer function is first corrected by the back-to-back calibration, to get $H(f) = H_{\mathrm{meas}}(f)/H_{\mathrm{cal}}(f)$. This is then transformed to the delay domain (with the inverse Fourier transform implemented as an IFFT) to obtain the impulse response $\tilde{h}(\tau)$. The instantaneous power delay profile, PDP, is then further delay-gated and noise-thresholded

$$P(\tau) = \left[\left| \tilde{h}(\tau) \right|^2 ; (\tau) : \left(\tau \leq \tau_{gate} \right) \wedge \left(|\tilde{h}(\tau)|^2 (\tau) \geq P_\lambda \right) \right] \quad (2)$$

or 0 if it does not fulfill these conditions. Here τ_{gate} is the delay gating value selected to avoid using long delay points and points with "wrap-around" effect of the IFFT, and P_λ is the noise threshold, which is chosen as 12 dB above the average noise level. The margin value was selected by analyzing the noise distribution in the PDP. Assuming the noise is *zero mean circularly symmetrically complex Gaussian* distributed $(N = N_I + jN_Q, N \sim CN(0, \sigma^2 \mathbb{I}))$, where $\mathbb{I}$ is an identity matrix; the amplitude of the noise follows a Rayleigh $(|N| = \sqrt{N_I^2 + N_Q^2}, |N| \sim Rayl(\sigma))$. Thus, the power follows an exponential distribution $(P = |N|^2, P \sim Exp(\Omega))$ [16], [72].

$$Pr\left(P \geq M\bar{\Omega}\right) = \int_{M\bar{\Omega}}^{\infty} \frac{e^{\frac{-P}{\bar{\Omega}}}}{\bar{\Omega}} dP = e^{-M} \quad (3)$$

where $\bar{\Omega} = \mathbf{E}(P) = P_N$ is the average noise power[7] and $M = 10^{M[dB]/10}$. This margin value ensures that the probability of accepting a delay bin with noise is roughly 10^{-7}, i.e., approximately one delay/angle bin within each snapshot. For the analysis of the delay parameters, $H(f)$ is multiplied with a Hann window before the Fourier transformation, since the sidelobes of the *sinc* function arising from the IFFT would lead to a significant distortion of the delay parameters.[8] Furthermore, the PDPs are computed with oversampling, since, e.g., the delay spread of a critically sampled PDP can deviate considerably from the value of the underlying continuous profile.[9]

All the above quantities depend on i, j, k, l, as well as the particular locations of the Tx and Rx. In case that measurements in multiple elevations are available, the PDPs are summed over j and l, as discussed in Section III. From the resulting elevation-integrated PDPs, we obtain the following three quantities:

1) *max-dir PDP:* we determine the horn azimuth combination $\hat{i}, \hat{k}$ that provides the largest total power (integrated over τ) and call it the max-dir PDP. The max-dir PDP, and all parameters derived from it below, depend on the beamwidth of the used horn.
2) *omni-directional PDP:* we combine all directional azimuth PDPs to synthesize a PDP that emulates the result we would get if we measured with an omni-directional antenna. This is done by the method of [73], where for each delay the maximum of the received power (over all azimuth angles) is identified, and the maxima are used to generate a total PDP.
3) *angular power spectrum*: by integrating the (directional) PDPs over delay, a discretized form of the angular power spectrum, APS, is obtained.[10]

From these quantities, we can further obtain condensed parameters:

- *Path gain, PG:* The PG is obtained by integrating the PDP over delay, providing the omni-directional PG or the max-dir PG, depending on which PDP is used as the basis for the computation. The path gain is of fundamental importance for the link budget, SNR, and thus capacity of a (single-stream) link. Scatter plots of the measurements, as well as functional fits, of PG as a function of distance will be provided in Section VII. However, two major caveats must be noted: (i) any fit is valid only within the range of distances in which it is done, (ii) the selection of Tx/Rx locations impacts the overall results. In our campaigns, measurement points were selected where it could be reasonably anticipated that the receive signal was strong enough for the channel to be estimated. Thus, the results are not suitable to assess the outage probability of cellular/WLAN/D2D

7. Further details on how to compute the average noise power will be explained in future papers.

8. For example, the second central moment of a (continuous) $|sinc|^2$ function over $[-\infty, \infty]$ is infinity.

9. Consider, for example, a PDP centered in the middle between two (critical) sampling points: its delay spread will be much larger than that of the same function centered on a sampling point.

10. Obviously, all measured PDPs and APSs are discrete; however, the figures below will show interpolated versions.

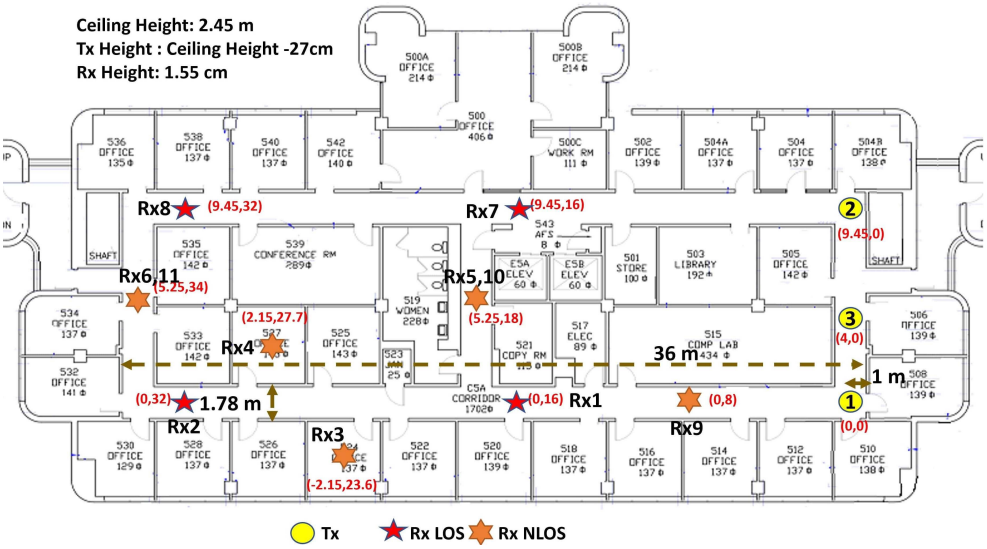

FIGURE 4. Map of the indoor environment.

THz systems, which should be based on measurements where at least one link end is placed at random, or on a regular grid.

- *RMS Delay Spread, DS:* The DS is defined as the second central moment of the PDP, and can thus be computed easily [16], though care must be taken to account for sidelobes stemming from the IFFT, and impact of MPCs whose delay is between sampling points, as discussed above. Depending on whether max-dir or omni PDP underlies the computation, we obtain the max-dir or omni DS. The DS is a common measure to describe the results of measurement campaigns, and can be tied (via uncertainty relations [74]) to the coherence bandwidth of the channel, and thus provide an indirect measure of the achievable frequency diversity.
- *Q-window:* Another quantity describing the delay dispersion is the Q-window, which quantifies the mininum window such that the ratio of energy of the impulse response within the window to that outside of it reaches a particular value Q. This quantity is most useful to assess OFDM and single-carrier systems where the equalizer taps are at regular locations, nT_c, $n = 1, 2, \ldots$ In both of these cases, Q describes the SIR, since the window contains useful signal, and the energy outside the window contains intersymbol interference.
- *Q-tapnumber:* A related quantity is the Q-tapnumber, which defines the minimum number of *arbitrarily-placed* taps (by enforcing that they are at integer multiples of the sampling interval) in order that the energy collected on those taps divided by those at other locations is Q. This quantity is useful to assess Rake receivers and equalizers with dynamically-placeable taps.
- *RMS angular spread, AS:* The AS quantifies the angular dispersion, and is thus a measure of the available angular diversity, possibility of spatial multiplexing, and interference between links with different horn directions. Thus, it is not possible to classify large angular dispersion as "beneficial" or "detrimental" to system performance; rather the particularities of the analyzed system configuration need to be taken into account. While the definition of angular spread (AS) as second central moment of the angular power spectrum (APS) is common in the literature, this definition suffers from ambiguity, since (due to the periodicity of the angular coordinates) the choice of the origin of the coordinate system has a major impact on the result. Instead, the definition of Fleury ([75], see also [16] and [17]) will be used in the following. In this definition, the range of possible values is [0, 1]; for small values the (dimensionless) Fleury AS has the same numerical value as a (suitably centered) second central moment expressed in radians. Finally, we note that the AS values are lower-bounded by the beamwidth of the horn used in our measurements.

V. THE MEASUREMENT ENVIRONMENTS

The environments in which the measurements are done govern which propagation processes occur, and what parameters of the MPC channel we can expect. Our measurements were done in the following sets of environments:

Indoor corridor and conference rooms: the indoor measurements were conducted in an office building. Tx and Rx were located either in a corridor (1.78m wide, 2.45 m high), or a variety of offices, see Figs. 4 and 5. The walls are made of post-and-drywall, and the windows are of the non-energy-saving type. In all the measurements, the Rx was at 1.55 m height while the Tx was at a height of 2.18 m, which corresponds to the height of a typical hotspot/indoor access point. The distance between Tx and Rx varied between 8 and 35 m. Overall, we measured 4 LoS links in the corridors, as well as 5 NLoS links in the corridors and 2 NLoS links in the

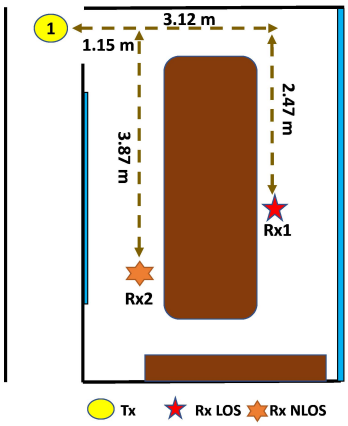

FIGURE 5. Map of the Conference room environment.

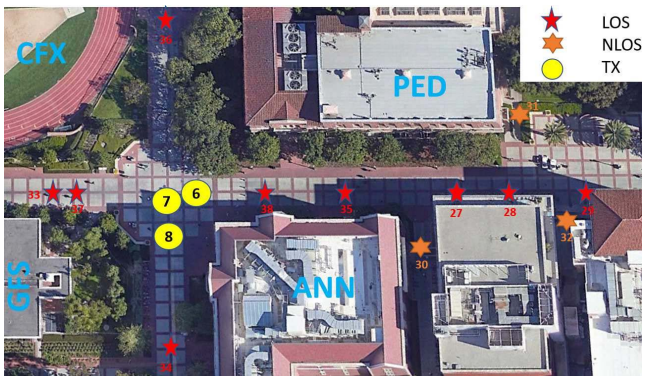

FIGURE 6. Map of the outdoor intersection environment.

offices. A map of the environments markings of the Tx and Rx locations is given in Figs. 5 and 4.

Outdoor plaza and street crossing: the D2D outdoor measurements were performed in two areas of the USC campus that are a plaza and a street crossing, respectively. The plaza encompasses an open area with concrete pillars, bounded by building walls on two sides, as well as a larger L-shaped space with trees, umbrellas, and tables. For the street intersection, there were buildings, and various amounts of vegetation, at three corners of the intersection, while at the fourth corner was a sports field surrounded by a metal fence. In all the measurements both Tx and Rx were at 1.6 m height. The distance between Tx and Rx varied between 1 and 93 m. Overall, we measured 12 LoS links in the plaza and 9 LoS links in the intersection, as well as 14 NLoS links in the plaza and 3 NLoS links in the intersection. A map of the environment marking the Tx and Rx locations is given in Figs. 6 and 7.

Street canyon and parking lot: the microcellular measurements were performed in an urban environment, with the Tx located at 11.6 m height essentially at the facade of a building, and the Rx located at various positions in a parking lot and in street canyons. Since the Tx was on a building facade (more precisely at openings in the building facade), its antenna was chosen to only illuminate a 120° sector. Different mounting positions on different walls of the building, pointing into different directions, were used. The 3D distance between the Tx and Rx varied between 20 and 85 m. Overall, we measured 13 LoS links and 13 NLoS links. A map of the environment with markings of the Tx and Rx locations is given in Fig. 8.

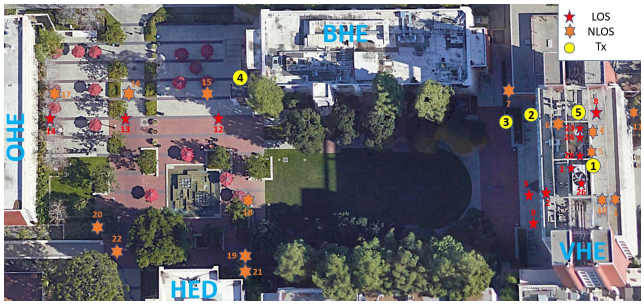

FIGURE 7. Map of the outdoor plaza for D2D environment.

FIGURE 8. Map of the outdoor plaza for microcellular environment.

More details about the environments, and listing of all measured links, can be found in [17], [18], [20], [21], respectively.

VI. SAMPLE RESULTS AND IMPACT OF SPECIFIC ENVIRONMENTS

The following figures show, for a number of sample cases, the angular delay power spectrum, ADPS, (where an integration over the transmit directions has been done, since four-dimensional descriptions are difficult to display), as well as the PDP and the APS at the Rx side derived as the marginal distributions of this ADPS.[11] The delays are given in units of meter (i.e., multiplied with speed of light) for easier geometric interpretation. From these results, we can intuit a number of insights into the relevant propagation processes.

Fig. 9 shows the results for a microcellular LoS link. From the plot, we can firstly see that - as expected - the LoS component carries the strongest power, arriving from 0° azimuth, and with a delay equal to the Euclidean Tx-Rx distance. We

11. Note that the PDP shown as the marginal distribution of the ADPS (i.e., ADPS integrated over all Rx angles) is defined slightly differently from the omni-PDP computed by the method of [73] as shown in the "standalone" PDP figures. However, the differences in the results are minor.

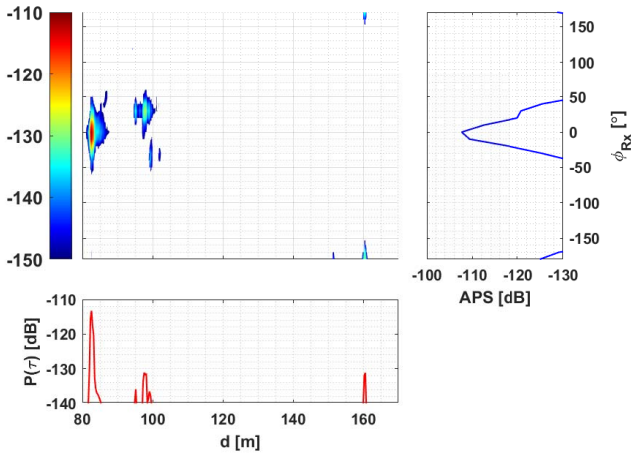

FIGURE 9. APDS of outdoor microcellular LOS link, TX1-Rx1 for $d_{Tx-Rx} = 82.5m$.

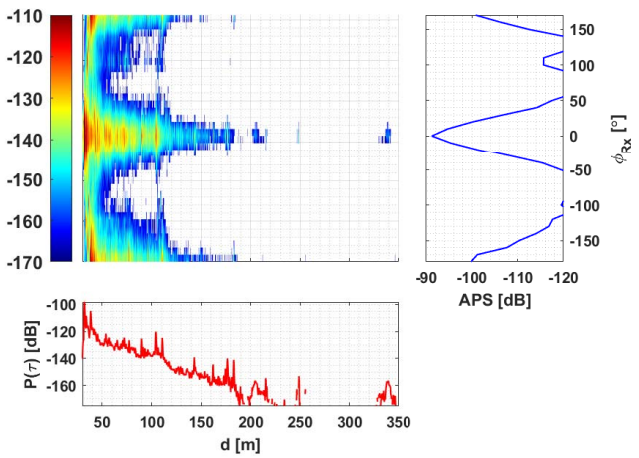

FIGURE 10. ADPS of indoor LoS link, TX2-Rx8. $d_{Tx-Rx} = 32m$.

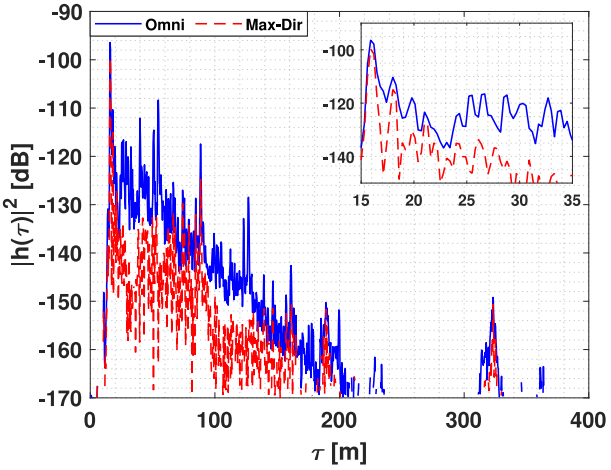

FIGURE 11. PDP of indoor LoS link, TX2-Rx8.

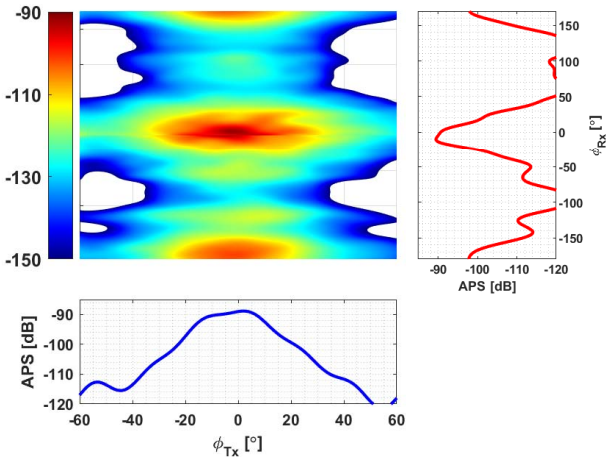

FIGURE 12. APS of indoor LoS link, TX2-Rx8.

also see that there are a number of significant MPCs at later delays (around 100 m) that come from different directions, and thus will be filtered out by a directional antenna pointing only in the LoS direction. Finally, reflections from the back (at $\phi_{RX} = 180°$) can be noted at a delay of 160 m. Please note that the reflections from the back are not the effects of the backlobe of the antenna, since such backlobes would show up at the LoS delay.

It is interesting to compare this outdoor LoS scenario to the indoor LoS example shown in Fig. 10, which was measured in a building corridor. We firstly note the significantly larger dispersion, both in the delay and the azimuth domain. This is related to the walls lining the corridor at the side and the back, thus giving rise to many MPCs and extended "ringing" of the echoes. Thus, even though the distance between Tx and Rx is much shorter than in the outdoor case, the delays of the echoes extend over a longer time (distance). We also note major differences in the APS: firstly, the main peak (around 0°) is broader than in the previous case because the waves are guided by the corridor, and thus reflected repeatedly at the sidewalls. Secondly, the power of the components arriving from the back ($\phi_{RX} = 180°$) is significantly higher than in the outdoor case, because the wall terminating the corridor is closer to the Rx, oriented perpendicular to the direction of LoS propagation, and has a high reflectivity.

Fig. 11 shows, in greater detail, the PDP, distinguishing between the omni-directional and the max-dir PDP for an indoor measurement. We can clearly see that omni case provides much richer multipath, but that even the max-dir case has a quite significant delay dispersion. The omni-PDP can be described as a single-exponential decay, with several additional pronounced discrete components. The joint APS at Tx and Rx side, depicted in Fig. 12, shows significant broadening of the main beams, and that energy arrives at the Rx both from the front and the back (note that the Tx only swept the 120° sector looking towards the Rx, so it does not illuminate the corridor wall behind it).

We next investigate the results for an outdoor NLoS scenario. An example ADPS from a D2D measurement is shown in Fig. 13. We firstly note that the PDP shows multiple

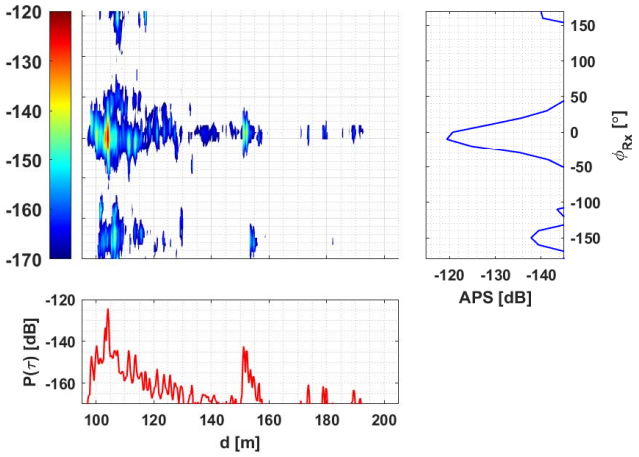

FIGURE 13. ADPS of outdoor D2D NLoS link, TX6-Rx32 for $d_{Tx-Rx} = 97.59m$.

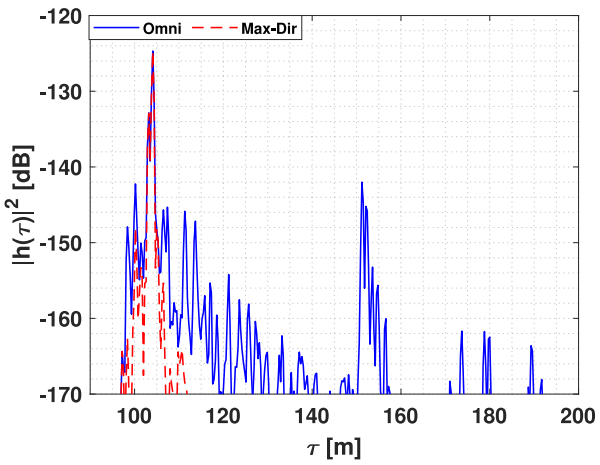

FIGURE 14. PDP of outdoor D2D NLoS link, TX6-Rx32.

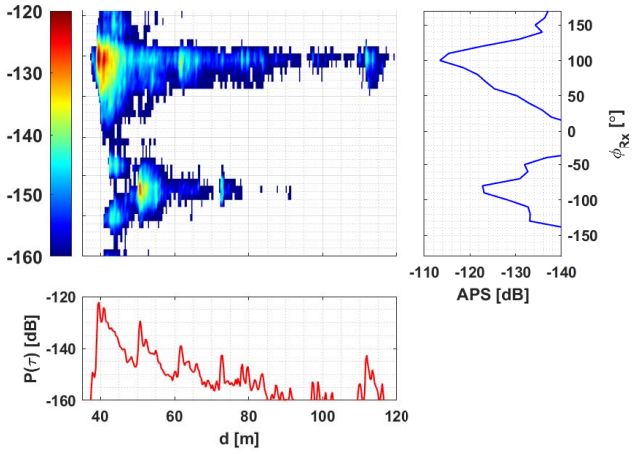

FIGURE 15. ADPS of indoor NLoS link, TX2-Rx6 for $d_{Tx-Rx} = 34.4m$.

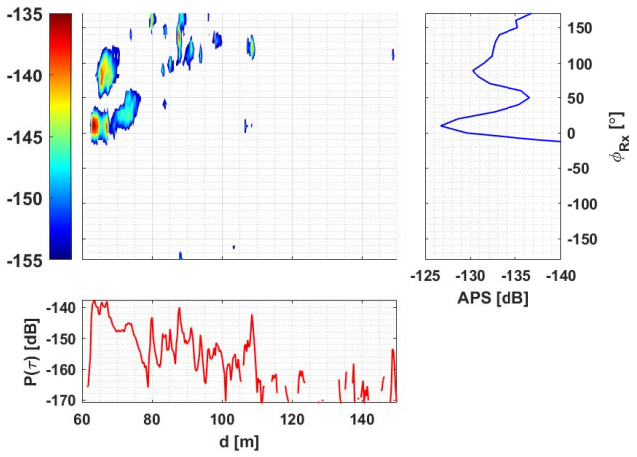

FIGURE 16. ADPS of outdoor NLoS link, TX3-Rx14 for $d_{Tx-Rx} = 62.6m$.

peaks, most with a considerable delay with respect to the direct distance between the Tx and Rx. The absence of a pronounced component at/near the LoS delay confirms that diffraction is not an efficient propagation process, as discussed in Section II. Note also that the strongest signal does not come from $\phi_{RX} = 0°$, which by definition is the geometrical LoS direction. We furthermore note significant components near 180°, which means that waves reflected by the building at the back of the Rx (buildings on the right side of the cross street in which the Rx is located) are important. More details of the PDP can be seen in Fig. 14. Again the omni-PDP shows a much larger multipath richness than the max-dir one.

Waveguiding also leads to interesting effects, both in outdoor environments (not shown for space reasons) and especially in indoor corridor environments, where it is very pronounced. A sample ADPS is shown in Fig. 15. In this case we use a coordinate system where 0/0 points in the direction of the corridor containing the Tx. We firstly observe that the strongest directions at the Rx are near 90° and - somewhat weaker - $-90°$. Thus, at the Rx the waves are coming down the corridor in which the Rx is located (and which is perpendicular to the corridor in which the Tx is located); with additional components that are first guided down the Rx corridor, and then reflected at the back wall of that corridor. Consistent with this interpretation, the first significant component with $\phi_{\mathrm{RX}} = -90°$ angle has a larger delay than the first component with the $\phi_{\mathrm{RX}} = 90°$. We also see a very pronounced cluster structure in the PDP, with each cluster decaying exponentially with a short time constant, and the power of the clusters decaying with a longer time constant. This is similar to the famous Saleh-Valenzuela (SV) model [76], though the cluster delays are deterministically periodic and not random as in the SV model.

Finally, we inspect an example of a microcellular NLoS scenario in an open square surrounded by buildings. Here the APS at the Rx (as seen in Fig. 16) shows several MPCs coming from positive angles, i.e., from scatterers located in the parking lot. Indeed, there were not only cars, but also multiple other objects like lantern masts, and signs, in the parking lot, which are effective reflectors at THz frequencies.

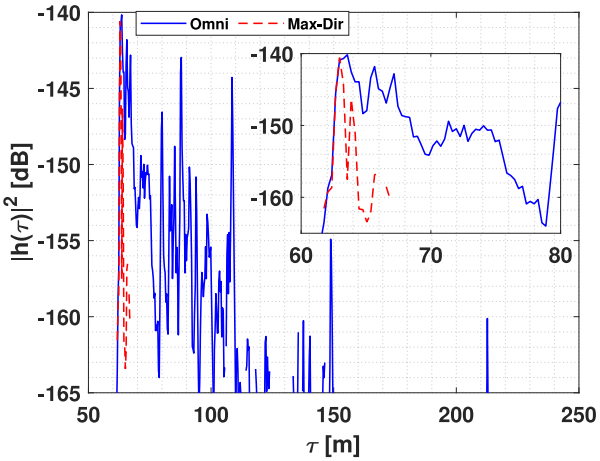

FIGURE 17. PDP of outdoor NLoS link, TX3-Rx14.

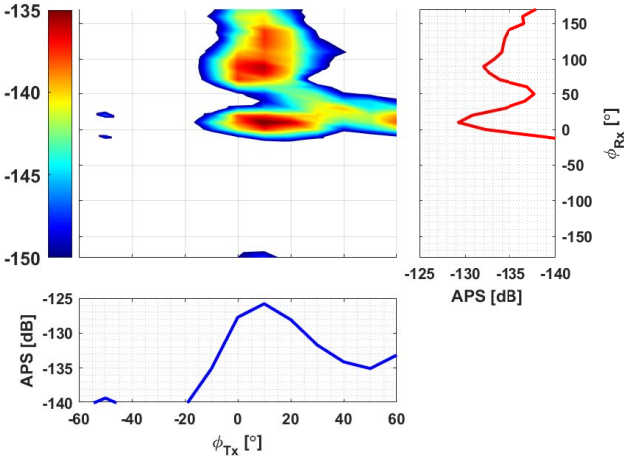

FIGURE 18. APS of outdoor NLoS link, TX3-Rx14.

In contrast, little power is coming from negative angles, which is where the building wall of USC Michelson Center for Convergent Bioscience (MCB) extends. The strongest - and first arriving - component has a *slightly* positive angle. We conjecture that it is a diffraction. While diffractions normally have extremely small power, in this case the diffraction angle is shallow. Furthermore, we see that the absolute power is indeed small; we conjecture that it is the largest one only because of the absence of buildings that could provide effective reflection processes larger than the diffracted component.

The NLoS characteristics also have a significant impact on localization. Most precision localization methods (including GPS) are either based on time-of-arrival, time-difference-of-arrival, or combinations thereof with signal strength and/or Direction of Arrival DoA. The discrepancy between nominal Euclidean distance between Tx and Rx on one hand, and the delay of the strongest (or the first measurable component) on the other hand thus impacts the accuracy of the measurements. Determination of which links are NLoS - information that can be used as basis of either discarding those links or subjecting them more advanced signal processing - is thus important for precision localization [77]. For this purpose, statistics of the excess delay of first/strongest components, and their correlation with other channel parameters such as excess path loss, need to be analyzed, which we will do in future work.

Since reflections are the dominant propagation process in NLoS situations, it is also interesting to investigate the impact of reflection coefficients and additional (passive) reflected objects on the received signal. We have performed such an experimental study in [20]. An example result is shown in Fig. 19, specifically showing the ADPS in an NLoS office channel in which the windows are either covered with blinds, or not. The presence of the blinds changes the strength of some of the longer-delayed echoes (10 m delay and more), indicating that the specific furnishing of a room might influence the ADPS. In further measurements (see [20] for details), we found that introduction of additional metallic objects can lead to an increase of the number of MPCs, and thus coverage and angular and delay diversity; however this can also possibly increase multi-user interference. The choice of the placement thus has to be handled carefully.

We finally analyze the potential impact of ground reflections. For short distances (< 20 m) and D2D settings, the elevation angle of the ground reflection is outside the main beamwidth of the horn antenna, and is thus significantly attenuated. For larger distances, ground reflection might be received, but cannot be resolved for 1 GHz bandwidth in the delay domain due to the small excess runlength (10 cm, which is significantly smaller than the resolvable bin-width of 1 ns $=$ 30 cm) of the ground reflection. We thus performed long-distance measurements with a bandwidth of 10 GHz. Since a full angular scan is neither possible for this bandwidth (due to the long measurement time) nor necessary to analyze the ground reflection of the LoS component, we only measured the PDP with the two horns pointing directly at each other. An example PDP in Fig. 20 shows a ground reflection at the excess delay to be expected from the geometry. We performed these measurements at a variety of distances between 15 and 70 m; the amplitude of the ground reflection is between 2 and 10 dB weaker than the LoS, with the specific attenuation depending on the surface structure at the reflection point (e.g., asphalt versus brick tiles). The ground reflection has little impact on the path loss measurements, which, within our distance measurement range, do not show a transition to the d^4 path loss law that is postulated when a ground reflection with reflection coefficient -1 destructively interferes with the LoS, see [16, Ch. 4].

VII. STATISTICAL RESULTS

For system design, the statistics of the different MPC-channel characteristics discussed in Section IV need to be analyzed. The following subsections and tables provide the "best fit" in terms of probability density function (for the distribution

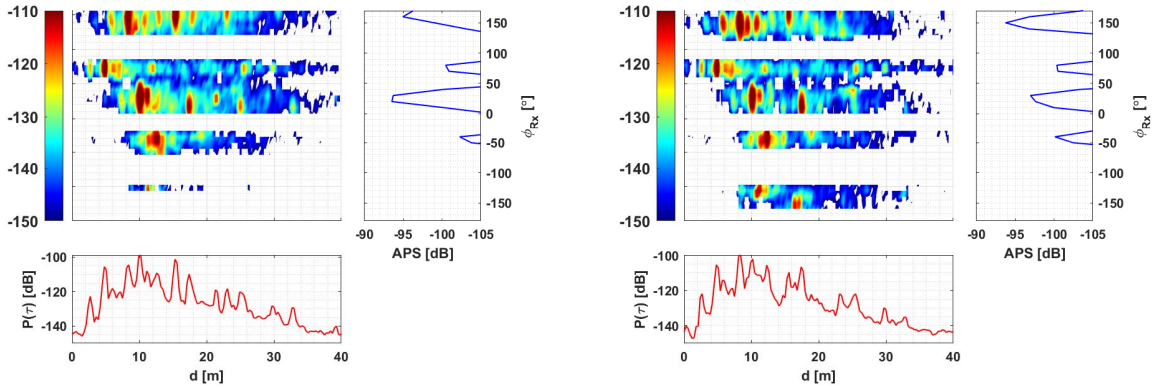

(a) with blinds (b) without blinds

FIGURE 19. ADPS of a link with and without reflectors, Conference room scenario (see [20] for details).

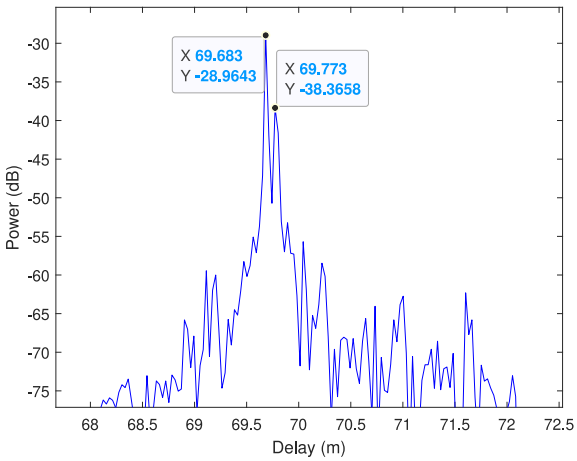

FIGURE 20. PDP of long-distance measurement (70 m link) with 10 GHz bandwidth.

of parameters over the ensemble of measured points), and the distance dependence of the parameters. Details about the fitting procedures, as well as the confidence intervals of the fitting parameters, are given in [17], [18], [21]. We stress again that the distance dependence of the parameters is only valid for the distance range in which the measurements were made.

A. PATH LOSS AND SHADOWING

Fig. 21 shows the path loss as a function of the Euclidean distance between Tx and Rx. In particular, Fig. 21a and b aggregate the results for LoS scenarios, and also shows the best fit for the $\alpha - \beta$ model

$$P_{\mathrm{Tx,dB}} + G_{\mathrm{Tx,dB}} + G_{\mathrm{Rx,dB}} - P_{\mathrm{Rx,dB}} = \alpha + 10\beta log_{10}\left(\frac{d}{1\mathrm{m}}\right) + \epsilon, \quad (4)$$

where ϵ is a lognormally distributed random variable with standard deviation σ^{ϵ}. We can see that in all environments, the path loss coefficient β is slightly smaller than 2, as can be expected for a LoS environment, due to the contribution of the LoS component itself that has path loss coefficient 2, and is augmented by other MPCs. We also see that the path loss is smaller in indoor than in outdoor environments, which is in line with the physical insight that a corridor (with highly reflecting, and (almost) continuous walls) guides power better than an open square or even a street canyon. Comparing the omni and the max-dir results, we see that the difference is relatively small, since most of the power is carried in the LoS component. The shadowing standard deviation is on the order of $1-2$ dB, indicating that an accurate prediction of the LoS signal strength can be realized. Again, this mainly rests on the dominance of the (highly predictable) LoS component compared to all other MPCs. If the antenna is not pointing towards the LoS component, or it is shadowed off by, e.g., a human body, the received power is dominated by indirect (i.e., non-LoS) MPCs, and exhibits considerably larger variations.

Figs. 21c and d show the path loss for the NLoS situations. We first of all notice that the path loss is almost always larger than the free-space path loss. Secondly, the excess path loss is significantly larger for the max-dir case than for the omni-directional case, indicating that a significant percentage of the energy comes from directions other than the max-dir direction.[12] Thirdly, for the microcellular case, the excess path loss increases with distance for the max-dir case, while it *decreases* for the omni-directional case. This indicates that the multi-path richness increases with increasing distance, leading to stronger contributions from different directions, again aligned with intuition. For the D2D case, the excess path loss decreases both for the max-dir and the omni case. For the indoor environment, trends are difficult to judge due to the relatively small range of distances (largest distance is only a factor 3 larger than the smallest distance). The shadowing standard deviation is significantly larger in the NLoS case than for LoS, ranging between 4 and 8 dB.

12. Of course, the receive SNR is higher in the max-dir case than in the omni case, due to the gains of the directional antennas at the two link ends.

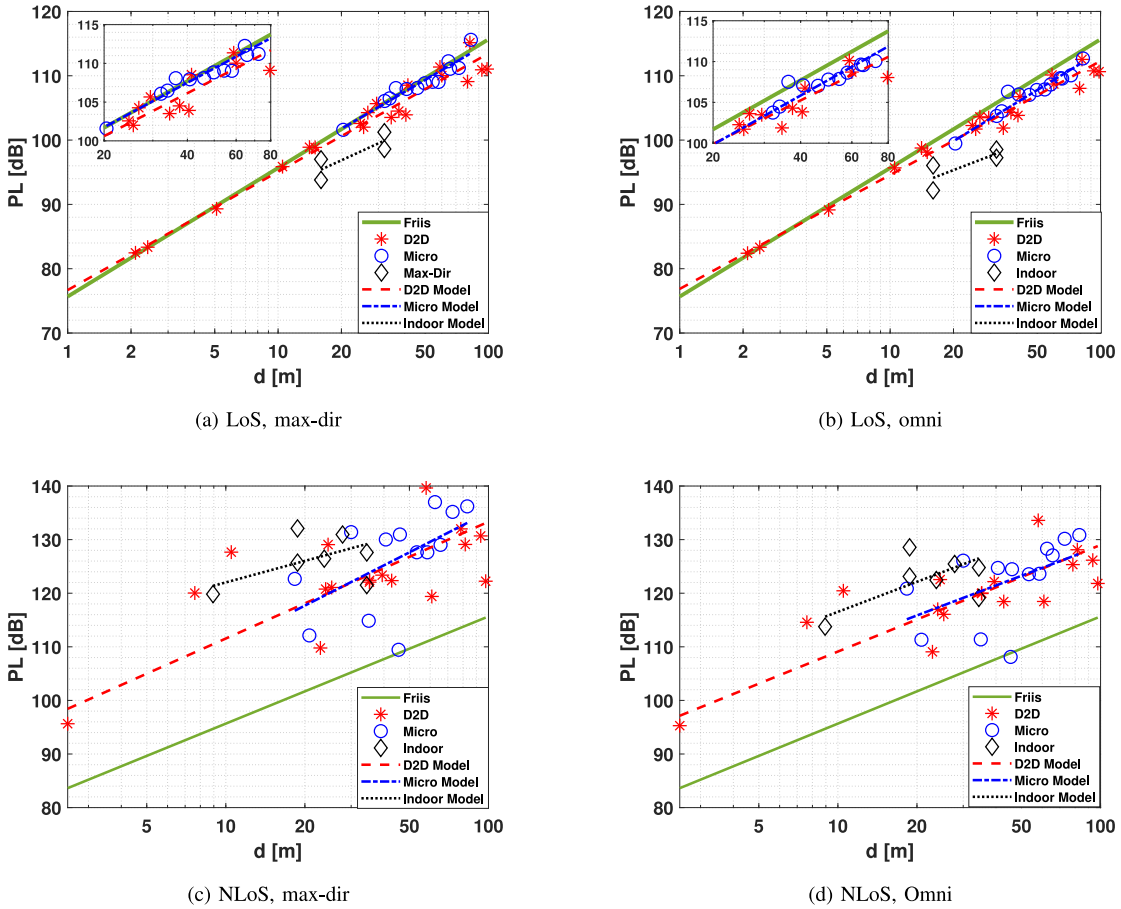

(a) LoS, max-dir

(b) LoS, omni

(c) NLoS, max-dir

(d) NLoS, Omni

FIGURE 21. Path loss as a function of distance.

TABLE 1. Path loss parameters in the different environments.

	$\alpha_{max-dir}$	$\beta_{max-dir}$	$n_{max-dir}$	α_{omni}	β_{omni}	n_{omni}	$\sigma^{\epsilon}_{max-dir}$	σ^{ϵ}_{omni}	**Range [m]**
Indoor LoS	77.35	1.5	1.62	79.01	1.25	1.49	1.69	1.67	[16-32]
D2D LoS	76.68	1.84	1.9	76.86	1.77	1.85	1.63	1.28	[1-100]
Microcell LoS	76.93	1.91	1.99	73.84	2	1.89	1.04	0.91	[20.4-82.5]
Indoor NLoS	108.67	1.33	3.93	97.91	1.86	3.61	4.36	4.32	[8.94-34.17]
D2D NLoS	89.76	2.18	3.16	89.22	1.99	2.93	7.53	5.37	[2-100]
Microcell NLoS	85.22	2.5	3.1	91.65	1.86	2.86	7.34	6.1	[18.3-83]

Table 1 summarizes the results for path loss coefficients and shadowing in all the environments. It shows the fitting parameters not only for the $\alpha - \beta$ model but also for the CI model (5), with the following formula:

$$P_{\mathrm{Tx,dB}} + G_{\mathrm{Tx,dB}} + G_{\mathrm{Rx,dB}} - P_{\mathrm{Rx,dB}} = FPSL(f, d_0) + 10nlog_{10}\left(\frac{d}{1\mathrm{m}}\right) + \epsilon, \quad (5)$$

where $FPSL(f, d_0) = -20\log_{10}(\frac{c}{4\pi f})$ is the Free space path loss at 1m distance, thus leaving only one parameter to optimize

Note that the shadowing variance is computed as the standard deviation with respect to the $\alpha - \beta$ fit.

B. DELAY DISPERSION

We next analyze the various measures for the delay dispersion, namely DS, Q-window, and Q-tapnumber. Fig. 22 shows the results in the various environments, separately for LoS and NLoS, and for max-dir and omni-directional antenna configuration. Due to the limited bandwidth and the Hann filter operation, the minimum measurable spread is around -93 dBs. For LoS situations, the DS generally remains below -80 dBs, while for NLoS, it can reach up to -68 dBs for the omni-directional case, and -75 dBs for the max-dir case. A comparison of these values to those at lower frequencies can be done mainly for the omni-case, since for the max-dir case the results depend on the beamwidth, and lower frequencies generally use larger beamwidth. We

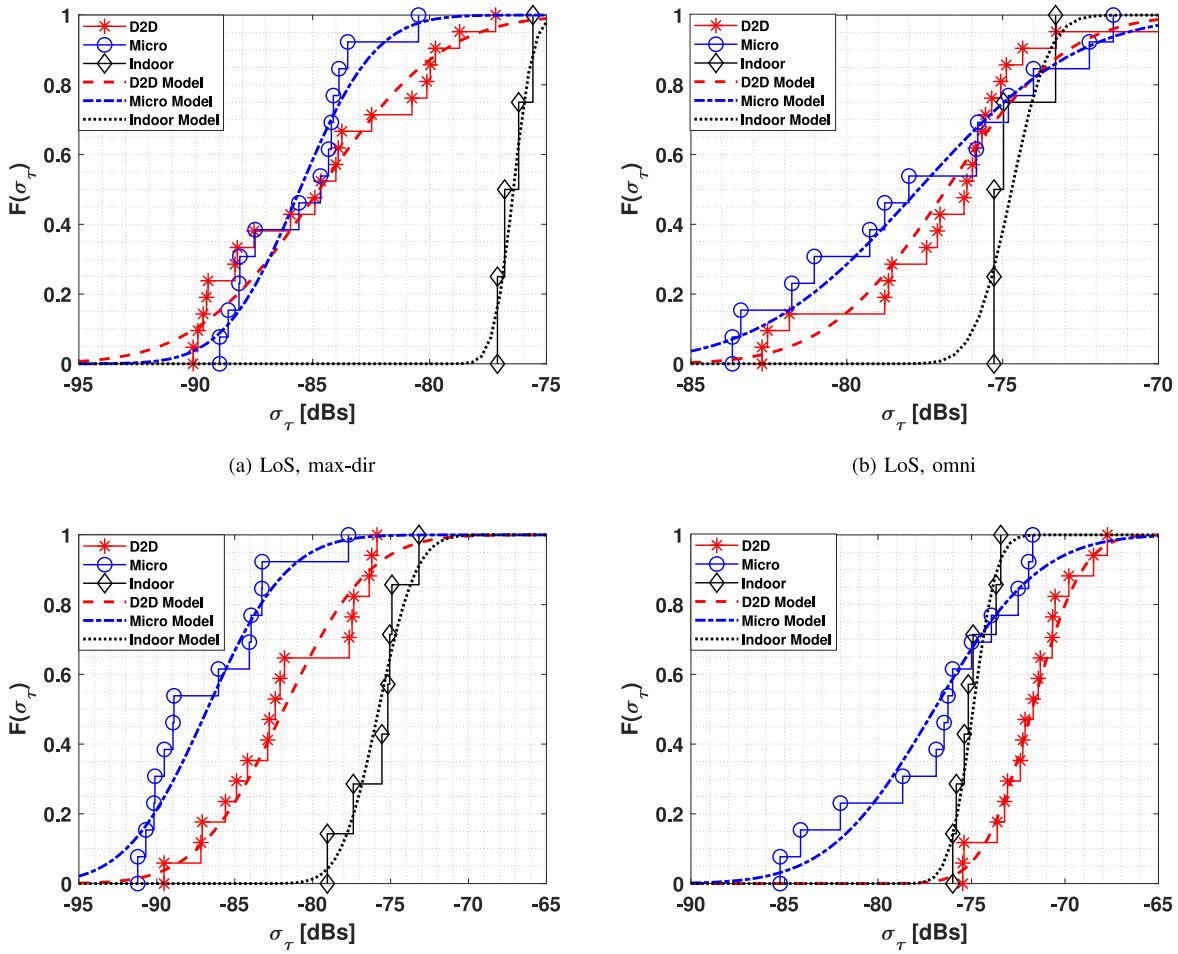

(a) LoS, max-dir

(b) LoS, omni

(c) NLoS, max-dir

(d) NLoS, Omni

FIGURE 22. CDF of the rms delay spread.

find that for the omni case, the results are on the same order as those obtained in similar environments (and similar antenna placements) at both mmWave [78] and cmWave frequencies [79].

The results also indicate that the coherence bandwidth is significantly smaller than the assumed system bandwidth of 1 GHz. This can be advantageous in terms of the available frequency diversity and thus robustness against small-scale fading. However, it also implies that the small-scale fading characteristics, and thus (digital) beamforming coefficients, vary significantly over the bandwidth. This not only means that (for a beamformer based on feedback) higher overhead for the feedback is required, but also that analog beamformers, which usually can only form a subcarrier-independent beampattern, may significantly underperform in a number of situations, a conclusion we will find confirmed in Section VIII.

When comparing the DS in the different environments, the microcellular case leads to the smallest DSs in all cases (LoS and NLoS, omni and max-dir). Outdoor D2D provides somewhat larger values, which can be explained by interacting objects being in the vicinity of both Tx and Rx, thus enabling richer multipath and stronger delayed components. Indoor environments provide the largest values; we conjecture that this is due to the specific type of indoor environment, namely a long corridor with well-reflecting walls, in which most of our indoor measurements were done. This conjecture is supported by the fact that the difference between outdoor and indoor DSs is largest for the LoS case (where the signal can be reflected multiple times between walls at the two ends of the corridor).

The CDF of the DS over the ensemble of measured points can be well fitted by a lognormal distribution, a finding that is consistent with the well-known model of

TABLE 2. σ_τ parameters in the different environments.

	$\mu_{max-dir}(dBs)$	$\sigma_{max-dir}(dBs)$	$\mu_{omni}(dBs)$	$\sigma_{omni}(dBs)$
Indoor LoS	-76.41	0.67	-74.71	0.95
D2D LoS	-84.7	4.16	-76.8	3.04
Microcell LoS	-85.54	2.53	-77.7	4.06
Indoor NLoS	-75.76	1.91	-74.91	1
D2D NLoS	-81.84	4.33	-71.76	2.09
Microcell NLoS	-86.76	4.06	-76.98	4.43

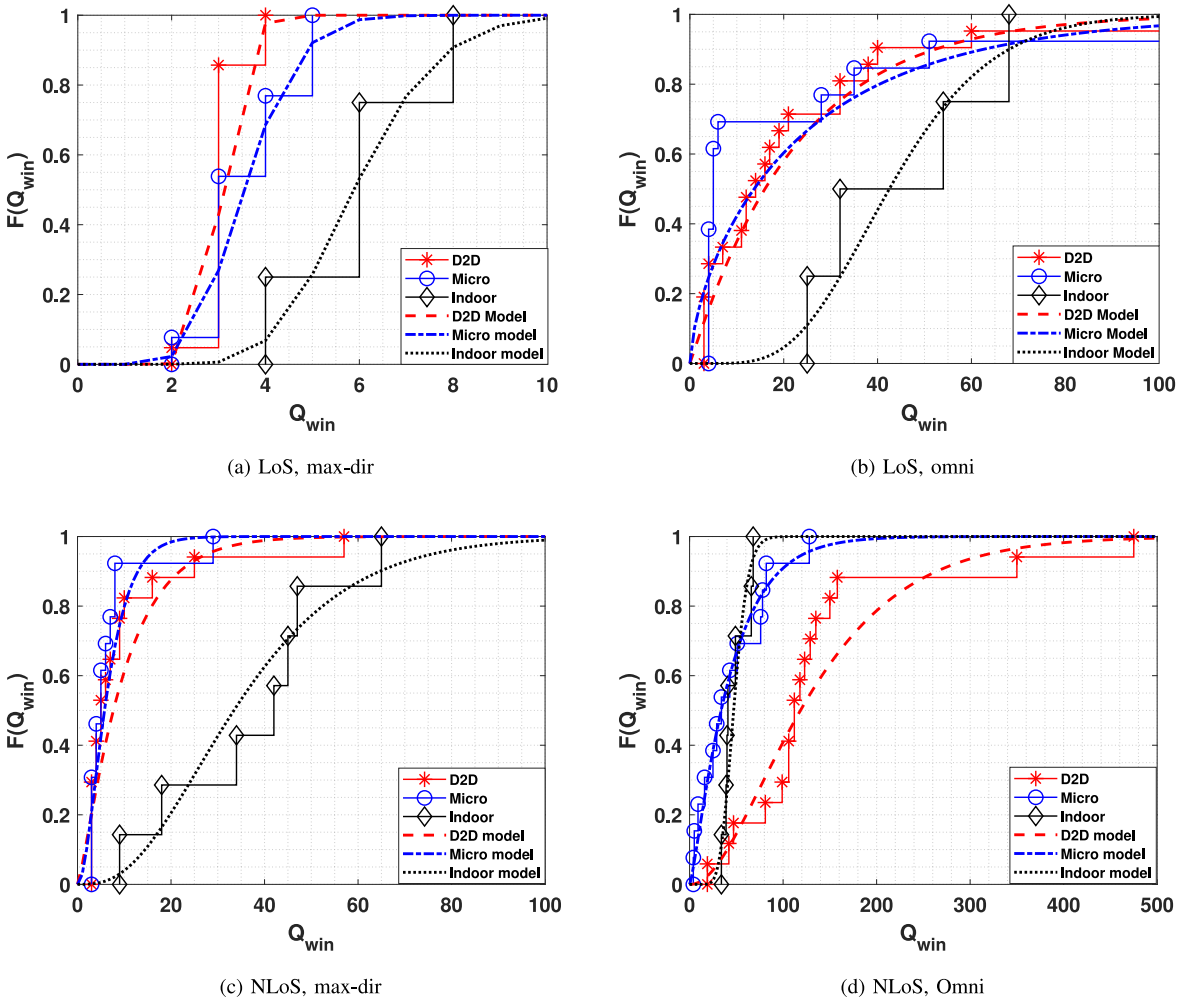

(a) LoS, max-dir

(b) LoS, omni

(c) NLoS, max-dir

(d) NLoS, Omni

FIGURE 23. CDF of the Q window, SINR = 15 dB.

Greenstein *et al.* [80] that has been validated in a variety of environments and frequency ranges. The DS also tends to increase with distance for most environments and antenna settings, but the confidence intervals of the estimated slopes are rather wide and often encompass both positive and negative values, for details see [17], [18]. Future measurements with larger numbers of points will be needed for a more definitive assessment.

We next turn to the Q-window, analyzing with a threshold SIR of 15, 20, and 25 dB. We consider here a tap size of 2ns, since we use a Hann window to obtain the impulse response (see Section IV), which broadens the main beam while suppressing sidelobes. CDFs are shown in Figs. 23, 24, and 25, respectively. As expected, the windows are larger for NLoS than for LoS, and for omni than for max-dir, and increase with increasing threshold SIR. Far more surprising is the range of absolute values of the windows: between 2 and 250 ns for the max-dir case (keeping in mind that the max-dir results are specific to the given antenna beamwidths) and up to 900 ns for the omni case. In the outdoor max-dir case, the Q-window is below about 80, 140, and 200 ns, respectively in about 90% of all cases, These results have significant impact on system design, in particular they indicate that the width of the cyclic prefix in an OFDM system has to be on the order of tens or even hundreds of ns, implying (for good spectral efficiency) at most hundreds of kHz of subcarrier spacing. Furthermore, for single-carrier systems with regularly-spaced equalizers, tens of, or even one hundred, taps are required, even in the max-dir case.

To model the statistical behavior of the Q-window parameter we use a Gamma distribution, which has the following probability density function (pdf):

$$f(x;\kappa,\lambda) = \frac{1}{\Gamma(\kappa)\lambda^{\kappa}} x^{\kappa-1} e^{-x/\lambda}, \tag{6}$$

where $\Gamma(x)$ is Euler's Gamma function. For a Gamma pdf, the mean and variance are calculated as:

$$E[x] = \kappa\lambda, \tag{7}$$

$$V[x] = \kappa\lambda^2, \tag{8}$$

where $E[\,\cdot\,]$, $V[\,\cdot\,]$ are the expected value and the variance of the random variable x, and κ, λ are the parameters of

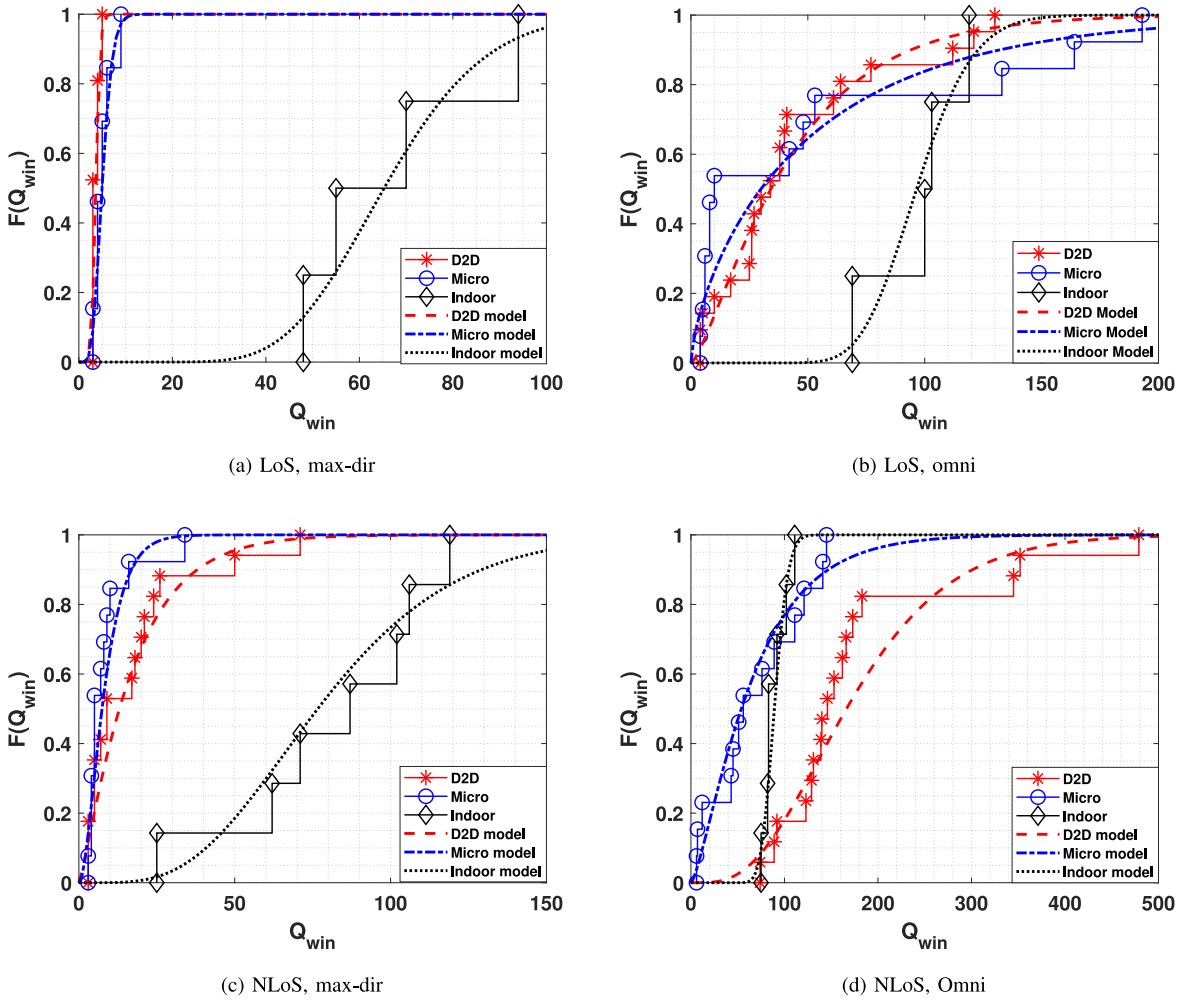

(a) LoS, max-dir

(b) LoS, omni

(c) NLoS, max-dir

(d) NLoS, Omni

FIGURE 24. CDF of the Q window, SINR = 20 dB.

TABLE 3. Q window parameters in the different environments.

	$\kappa^{15dB}_{max-dir}$	$\lambda^{15dB}_{max-dir}$	κ^{15dB}_{omni}	λ^{15dB}_{omni}	$\kappa^{20dB}_{max-dir}$	$\lambda^{20dB}_{max-dir}$	κ^{20dB}_{omni}	λ^{20dB}_{omni}	$\kappa^{25dB}_{max-dir}$	$\lambda^{25dB}_{max-dir}$	κ^{25dB}_{omni}	λ^{25dB}_{omni}
Indoor LoS	17.14	0.35	6.59	6.79	15.15	4.41	26.3	3.72	8145.5	0.004	1000.4	0.13
D2D LoS	53	0.06	1.05	22.29	23.78	0.15	1.38	31.98	8.2	0.62	2.05	37.45
Microcell LoS	15.09	0.24	0.65	37.53	8.63	0.6	0.68	76.74	7.29	0.91	1.12	60.08
Indoor NLoS	3.28	11.32	15.66	3.07	5.3	15.4	60.27	1.49	10.67	9.79	184.88	0.68
D2D NLoS	1.29	7.83	2.2	63.15	1.24	14.05	4.07	44.5	1.16	50.44	4.97	47.67
Microcell NLoS	2.18	3.11	1.29	34.58	2.11	4.15	1.41	49.27	2.32	4.43	1.74	64.15

the distribution, whose values in different environments are tabulated in Table 3.

We finally turn to the Q-tapnumber. Again we observe similar trends as for the Q-window, namely that max-dir PDPs have a much smaller number of relevant taps, and that the number of taps is lower in LoS than in the NLoS situations - not because there are fewer MPCs, but because the LoS component is much stronger, and thus fewer taps are needed to collect a total percentage of energy. In absolute terms, the number of taps is much smaller than the length of the Q-window divided by the delay binwidth, which indeed indicates that the PDPs are sparse in the sense that the *percentage* of taps containing significant energy is small; however they are not sparse in the sense that the *absolute number* of taps is small. For the outdoor cases, the number of taps at the (approximate) 90% level are 10, 25, and 40, respectively - considerably smaller than the Q-windows, but still a significant number.

Similar to the previous parameter, we used a Gamma distribution to model the statistical behavior of the Q-tapnumber and the parameters of the distribution are tabulated in Table 4.

C. ANGULAR DISPERSION

We next move to measures for the angular dispersion, in particular the AS. For the D2D scenarios (both outdoors

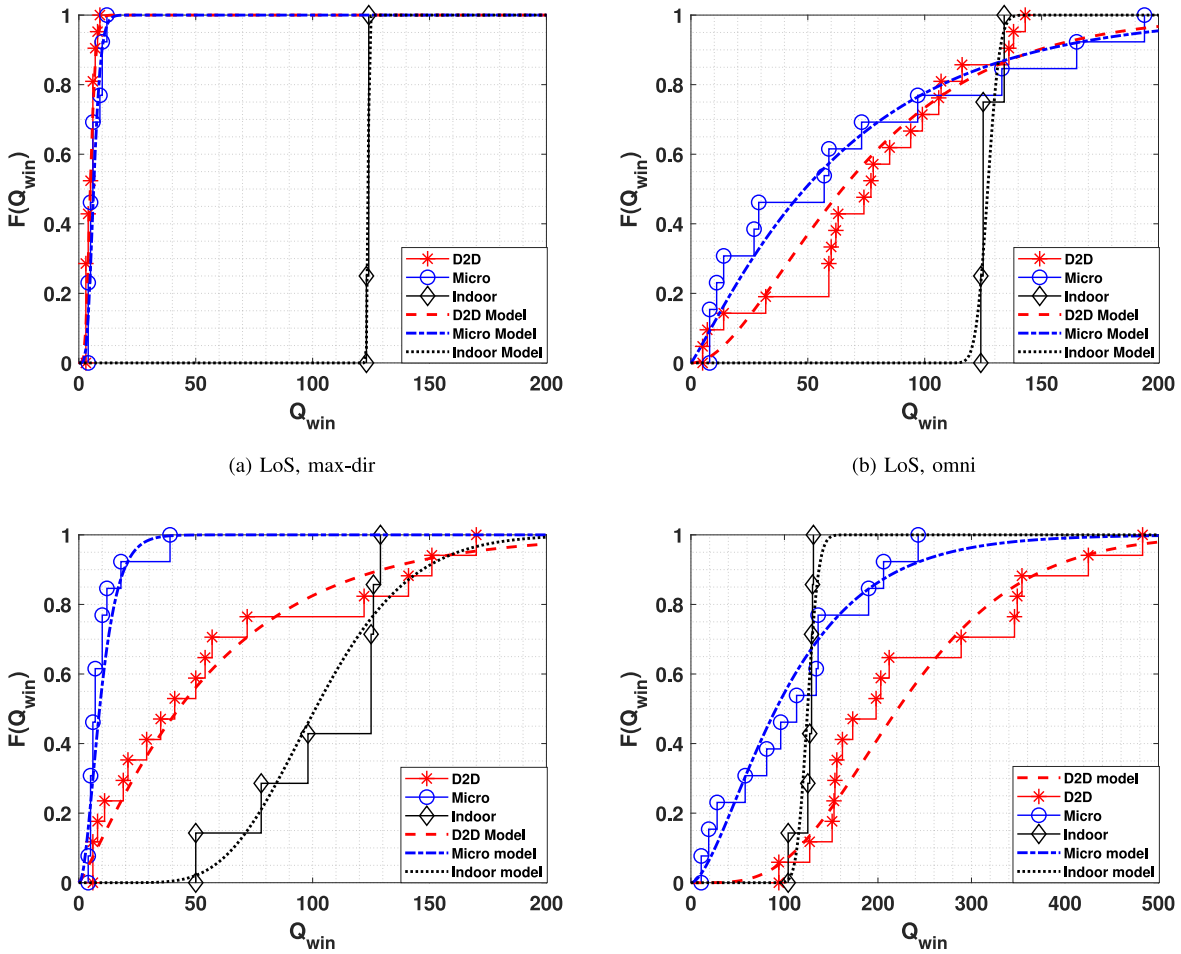

(a) LoS, max-dir

(b) LoS, omni

(c) NLoS, max-dir

(d) NLoS, Omni

FIGURE 25. CDF of the Q window, SINR = 25 dB.

TABLE 4. Q-tapnumber parameters in the different environments.

	$\kappa^{15dB}_{max-dir}$	$\lambda^{15dB}_{max-dir}$	κ^{15dB}_{omni}	λ^{15dB}_{omni}	$\kappa^{20dB}_{max-dir}$	$\lambda^{20dB}_{max-dir}$	κ^{20dB}_{omni}	λ^{20dB}_{omni}	$\kappa^{25dB}_{max-dir}$	$\lambda^{25dB}_{max-dir}$	κ^{25dB}_{omni}	λ^{25dB}_{omni}
Indoor LoS	11.94	0.34	8.56	2.54	4.7	3.62	29.44	1.87	24.27	2.13	118.22	0.78
D2D LoS	31.54	0.07	3.49	1.6	8.99	0.33	2.92	5.32	7.77	0.54	2.85	13.83
Microcell LoS	14.59	0.18	7.02	0.64	14.85	0.25	3.41	2.86	7.97	0.69	3.73	5.98
Indoor NLoS	4.47	5.88	15.37	2.71	6.08	8.66	35.7	2.01	11.33	7.29	103.73	1.01
D2D NLoS	3.63	1.2	2.52	23.4	2.13	4.19	4.92	20.12	2.81	6.49	8.56	16.29
Microcell NLoS	2.35	2.26	1.39	23.29	1.95	3.9	1.49	35.11	2.08	4.52	1.95	37.55

and indoors), there is no need to distinguish between AS at the Tx and Rx. For those scenarios, the CDFs of the AS are shown in Fig. 29. The logarithm of the AS is bounded on the lower limit by approximately -0.8, due to the finite beamwidth of the horn antennas. When analyzing the CDFs of the AS, we can observe 3 clusters of curves in the LoS case: (i) AS at the microcellular and indoor Tx (i.e., the BS or access point); due to the elevated position and the limited angular range during scanning, the values are small and range from -0.8 to -0.6 for LoS. In the NLoS case, the variations are much larger (-0.8 to -0.2). (ii) AS for the microcell Rx, and the D2D Rx and Tx (remember that in the D2D case, there is on average no difference between the environment that Tx and Rx see). Here, in the LoS case values vary between -0.8 and -0.05, with a mean around -0.5; in the NLoS case it varies between -0.6 and 0. The fact that we observe larger values of the AS can be explained by the richer scattering environment around the (outdoor) device at 1.6 m height, compared to an elevated BS. (iii) indoor Rx shows the largest AS (between -0.2 and 0, due to strong signals incident from the front and the back (again, due to the corridor structure in which we measured).

The CDFs can be fitted well by lognormal distributions, as shown in Fig. 29; the parameters of these distributions are given in Table 5.

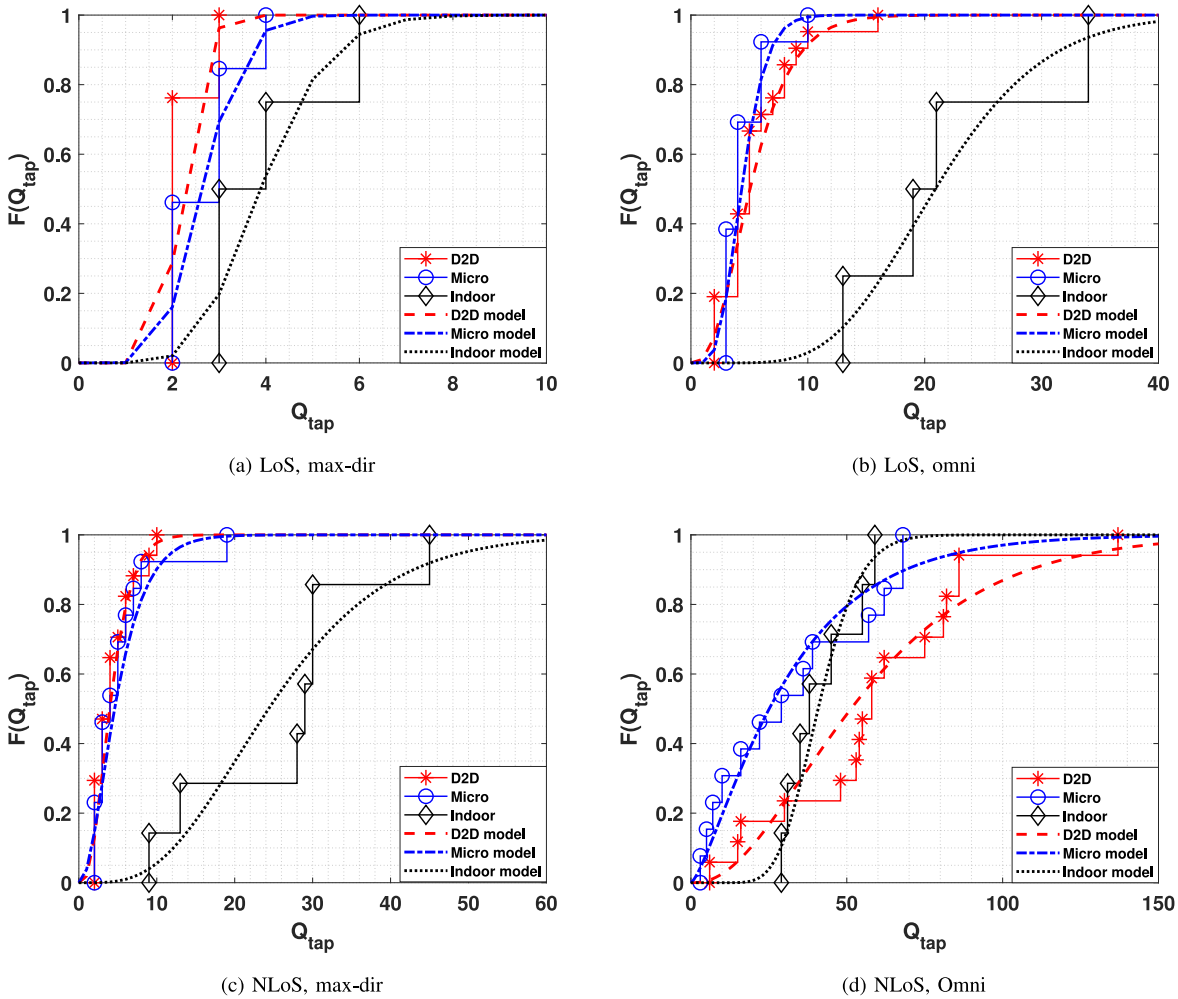

(a) LoS, max-dir

(b) LoS, omni

(c) NLoS, max-dir

(d) NLoS, Omni

FIGURE 26. CDF of the Q-tapnumber, SINR = 15dB.

TABLE 5. $\log_{10}(AS)$ parameters in the different environments.

	μ_{Tx}/μ_{D2D}	σ_{Tx}/σ_{D2D}	μ_{Rx}	σ_{Rx}
Indoor LoS	-0.7	0.05	-0.12	0.07
D2D LoS	-0.49	0.2	N.A.	N.A.
Microcell LoS	-0.73	0.06	-0.53	0.15
Indoor NLoS	-0.6	0.21	-0.14	0.06
D2D NLoS	-0.23	0.17	N.A.	N.A.
Microcell NLoS	-0.5	0.19	-0.36	0.21

VIII. SYSTEM PERFORMANCE

The impact of the angular dispersion on the system performance depends on the specific beamforming algorithms. In [19], we evaluated both analog and digital beamforming with measured outdoor D2D propagation channels for both "piconet-controller" and "peer-to-peer" scenarios. In the former case, different devices are all talking to a single device, e.g., a piconet controller, which uses beamforming to spatially separate the different users. In the latter case, pairs of devices are talking to each other, and pointing beams towards each other.

For the analog beamformer, we assume that the receiving device simply selects the beam that provides the highest power of the desired signal. This beam selection takes into account that an analog beamformer can only form a beam that is valid for all incident signals, but it is actually more restrictive in that it allows only the selection of a fixed beam and not the forming of an arbitrary beamshape. It is, however, a simple structure and in line with simple phased arrays in cellular handsets that typically also step (and not sweep) over different angles.

For the digital beamformer, we assume that all 36 receive signals (one from each of the Rx antenna directions) are processed with either maximum-ratio combining (MRC). zero-forcing (ZF), or minimum mean square error (MMSE). Since different beamformers on different subcarriers (or more generally, different parts of the band) are possible, better performance can be anticipated.

Figs. 30-32 compare the performance achieved with those beamforming schemes in a piconet controller and a peer-to-peer scenario, respectively. The results in Fig. 30 assume a network consisting of peer devices (i.e., D2D channels),

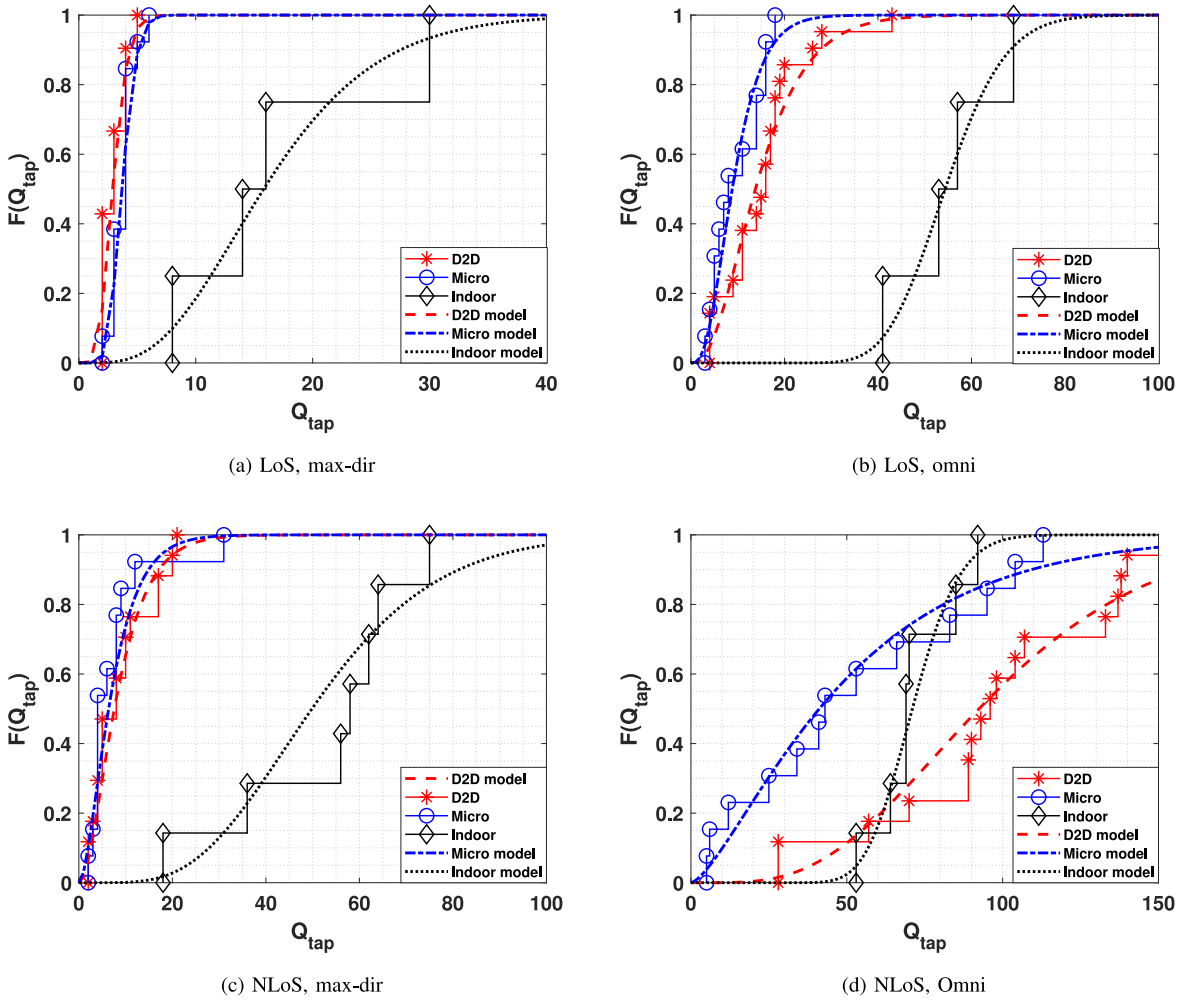

(a) LoS, max-dir

(b) LoS, omni

(c) NLoS, max-dir

(d) NLoS, Omni

FIGURE 27. CDF of the Q-tapnumber, SINR = 20dB.

where one of the peer devices serves as piconet controller. In this example, we see that in two cases (PnC7 and PnC8), analog beamformer provides a capacity that has a similar behavior (as function of the transmit power) as digital beamforming, and generally shows an offset of about 1-2 bit/s/Hz; this might be an acceptable loss in many situations, given the much lower complexity of the analog beam selection. However, we also see that in one example (PnC5), the analog beamformer has a much worse performance; capacity as function of SNR essentially saturates at a low level, as does digital MRC combining. In contrast, for digital beamforming with ZF or MMSE, capacity increases with the Tx power. This is due to the fact that several devices are in one beam of the piconet controller, so that their transmissions collide. Better scheduling would reduce this problem, but still the use of beam selection instead of creation of complex weights that optimize reception, exerts a significant performance penalty. Similar results occur in a microcellular setup where multiple devices access the BS, see Fig. 31.

In the P2P scenario, the capacity considerably depends on the directions into which the interfering devices transmit. Since the different devices are assumed not to coordinate their transmissions with each other, we can assume that transmissions occur into random directions. For this case, Fig. 32 shows the CDF of the capacity (over the ensemble of interference directions), for a variety of devices. Only analog beamforming is considered in this case. We can see that the considerable angular dispersion leads to more interference than what one could expect if THz links consisted only of LoS components. More examples and details of the configurations are discussed in [19].

IX. CONCLUSION

This paper has provided an overview of extensive channel sounding campaigns in the THz band, specifically at 145 GHz. We have described our measurement setup, the measurement environments (outdoor microcell, outdoor D2D, and indoor), and the parameters extracted from the measurements. Most importantly, we surveyed the numerical results for path loss, delay dispersion, and angular dispersion. Some of the key insights are as follows:

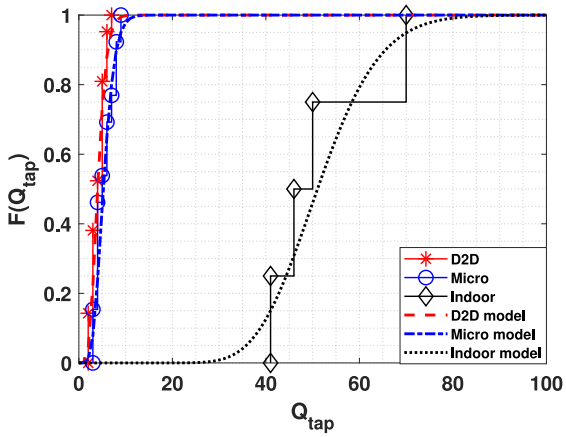

(a) LoS, max-dir

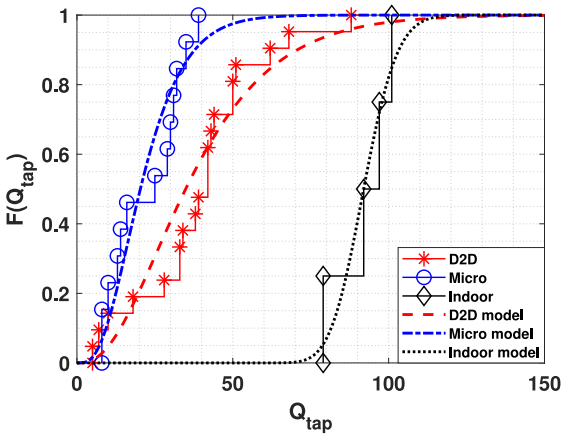

(b) LoS, omni

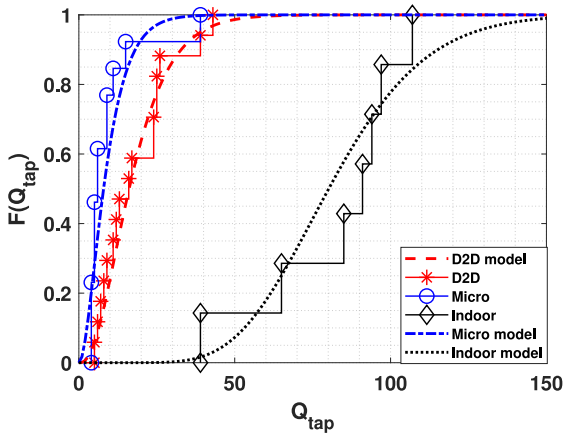

(c) NLoS, max-dir

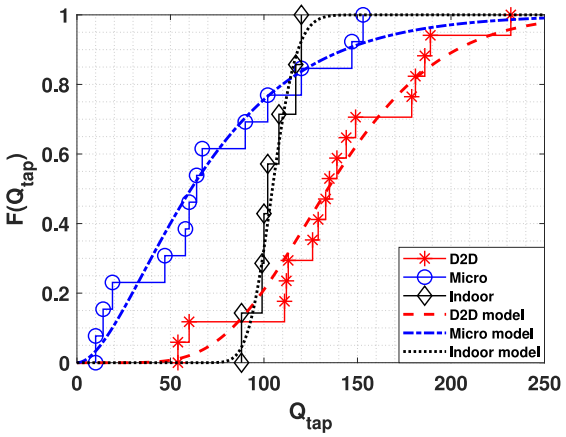

(d) NLoS, Omni

FIGURE 28. CDF of the Q-tapnumber, SINR = 25dB.

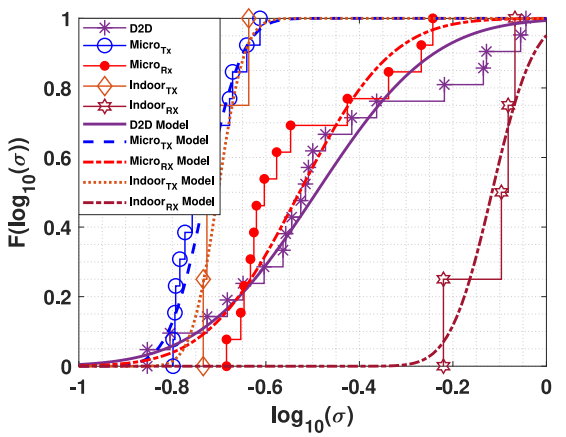

(a) σ° for LoS

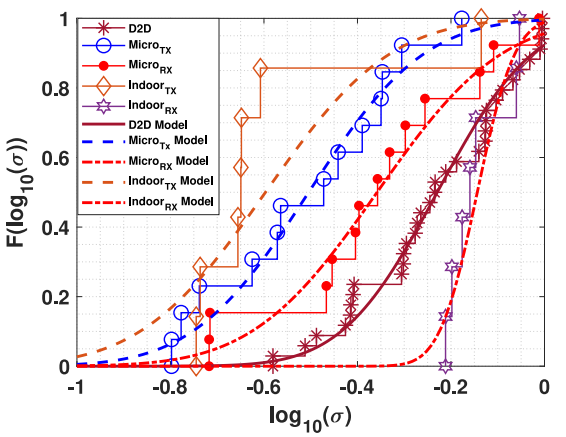

(b) σ° for NLoS

FIGURE 29. CDF of the AS.

- For LOS, the path loss coefficient is on the order of 1.8, similar to what is observed in lower frequency bands. The impact of ground reflections is minor in the situations we analyzed.
- For NLOS, the excess path loss (compared to free-space) is on the order of 10-30 dB, and generally decreases with increasing distance between Tx and Rx in particular in the omni-directional case, due to the

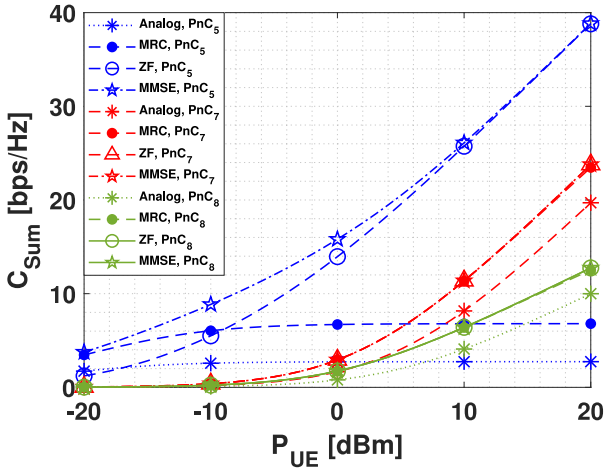

FIGURE 30. Comparison of digital and analog beamforming in a piconet controller scenario.

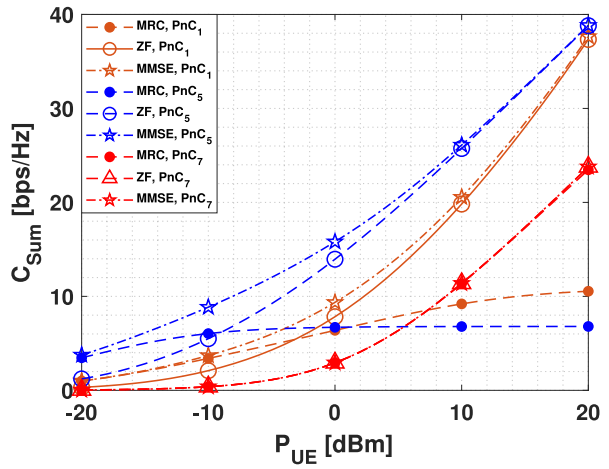

FIGURE 31. Comparison of digital beamforming in a piconet controller scenario.

rich multipath. However, this result does not incorporate heavily shadowed locations.

- For the considered beamwidth ($\approx 13°$), delay dispersion is considerable. When considering the max-dir delay spread, values are up to 30 ns in D2D and indoor environments, and 10 ns in microcellular environments, with values up to 150 ns for the omni-directional case.
- Q-windows, which indicate the necessary length of cyclic prefixes, can be tens or even hundreds of ns long for the max-dir case (and larger for the omni-case). Q-tapnumbers, which indicate the required number of arbitrarily spaced equalizer taps, is considerably lower than that, indicating sparsity of the channels, but still tens of taps might be required for, e.g., 20 dB signal-to-self-interference ratio.
- Angular spreads are smallest at elevated BSs, either indoor or outdoor. At the UE location, which is usually surrounded by scattering objects, large ASs (many multiples of the antenna beamwidth) were observed.

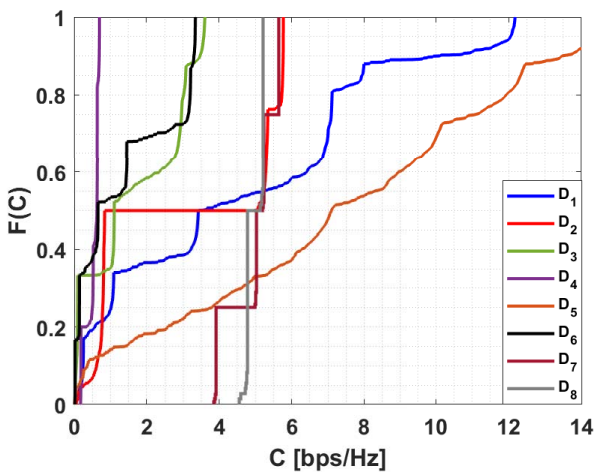

FIGURE 32. Comparison of analog beamforming in a P2P scenario.

- The angular dispersion has a significant impact on the multi-user capacity. For dispersive channels, digital beamforming to separate users coming from similar directions results in significant performance advantages compared to simple beam selection.

While the measurement campaigns are among the largest ever done in this frequency range, the number of points and variety of investigated environments is still quite limited. Thus, the results presented here can be considered a useful starting point for reality-based values of system design and performance assessment, but will be augmented by future measurement campaigns.

ACKNOWLEDGMENT

The authors thank Zihang Cheng, Shadi Abu-Surra, Gary Xu, Mark Rodwell, and Sundeep Rangan for helpful discussions, Ahmed S. Almaiman for his help with the RoF setup, and Revanth Kondaveti, Ashish Kumar, Eshan Bhagat, Rakesh N S Rao, Shahid M. Shaikbepari, Shreyas Rao, Arjun Hariharan, and Arun Moni Nair for their help during the measurement campaigns.

REFERENCES

[1] H. Tataria, M. Shafi, A. F. Molisch, M. Dohler, H. Sjoland, and F. Tufvesson, "6G wireless systems: Vision, requirements, challenges, insights, and opportunities," *Proc. IEEE*, vol. 109, no. 7, pp. 1166–1199, Jul. 2021.

[2] L. Zhang, Y.-C. Liang, and D. Niyato, "6G visions: Mobile ultra-broadband, super Internet-of-Things, and artificial intelligence," *China Commun.*, vol. 16, no. 8, pp. 1–14, Aug. 2019.

[3] T. S. Rappaport *et al.*, "Wireless communications and applications above 100 GHz: Opportunities and challenges for 6G and beyond," *IEEE Access*, vol. 7, pp. 78729–78757, 2019.

[4] E. C. Strinati *et al.*, "6G: The next frontier: From holographic messaging to artificial intelligence using subterahertz and visible light communication," *IEEE Veh. Technol. Mag.*, vol. 14, no. 3, pp. 42–50, Sep. 2019.

[5] A. Clemm, M. T. Vega, H. K. Ravuri, T. Wauters, and F. De Turck, "Toward truly immersive holographic-type communication: Challenges and solutions," *IEEE Commun. Mag.*, vol. 58, no. 1, pp. 93–99, Jan. 2020.

[6] M. J. Marcus, "Progress in opening access to spectrum above 100 GHz," *IEEE Wireless Commun.*, vol. 26, no. 2, pp. 2–3, Apr. 2019.

[7] S. Li, Z. Zhang, B. Rupakula, and G. M. Rebeiz, "An eight-element 140-GHz wafer-scale IF beamforming phased-array receiver with 64-QAM operation in CMOS RFSOI," *IEEE J. Solid-State Circuits*, vol. 57, no. 2, pp. 385–399, Feb. 2022.

[8] A. Simsek, S.-K. Kim, and M. J. Rodwell, "A 140 GHz MIMO transceiver in 45 nm SOI CMOS," in *Proc. IEEE BiCMOS Compound Semicond. Integr. Circuits Technol. Symp. (BCICTS)*, 2018, pp. 231–234.

[9] Z. Griffith, M. Urteaga, and P. Rowell, "A compact 140-GHz, 150-mW high-gain power amplifier MMIC in 250-nm InP HBT," *IEEE Microw. Wireless Compon. Lett.*, vol. 29, no. 4, pp. 282–284, Apr. 2019.

[10] L. John, A. Tessmann, A. Leuther, P. Neininger, T. Merkle, and T. Zwick, "Broadband 300-GHz power amplifier MMICs in InGaAs mHEMT technology," *IEEE Trans. THz Sci. Technol.*, vol. 10, no. 3, pp. 309–320, May 2020.

[11] J. Federici and L. Moeller, "Review of terahertz and subterahertz wireless communications," *J. Appl. Phys.*, vol. 107, no. 11, 2010, Art. no. 111101.

[12] T. Kleine-Ostmann and T. Nagatsuma, "A review on terahertz communications research," *J. Infrared Millimeter Terahertz Waves*, vol. 32, pp. 143–171, Jan. 2011.

[13] I. F. Akyildiz, J. M. Jornet, and C. Han, "Terahertz band: Next frontier for wireless communications," *Phys. Commun. J.*, vol. 12, pp. 16–32, Sep. 2014.

[14] C. E. Shannon, "A mathematical theory of communication," *Bell Syst. Tech. J.*, vol. 27, no. 3, pp. 379–423, 1948.

[15] A. Goldsmith, S. A. Jafar, N. Jindal, and S. Vishwanath, "Capacity limits of MIMO channels," *IEEE J. Sel. Areas Commun.*, vol. 21, no. 5, pp. 684–702, Jun. 2003.

[16] A. F. Molisch, *Wireless Communications*, 2nd ed. Chichester, U.K.: IEEE Press Wiley, 2011.

[17] N. A. Abbasi *et al.*, "Thz band channel measurements and statistical modeling for urban D2D environments," Jul. 2021, *arXiv:2109.13693*.

[18] N. A. Abbasi *et al.*, "THz band channel measurements and statistical modeling for urban microcellular environments," Jan. 2022, *arXiv:2112.01770*.

[19] J. Gomez-Ponce, N. A. Abbasi, Z. Cheng, and A. F. Molisch, "Directional characteristics of THz outdoor channels—Measurement and system performance implications," in *Proc. Asilomar Conf.*, 2021, pp. 658–663.

[20] J. Gomez-Ponce *et al.*, "Impact of common reflecting and absorbing building materials on THz multipath channels," *Radio Sci.*, vol. 57, no. 2, 2022, Art. no. e2021RS007412. [Online]. Available: https://agupubs.onlinelibrary.wiley.com/doi/abs/10.1029/2021RS007412

[21] N. A. Abbasi *et al.*, "Measurement and modeling of THz propagation channels in indoor environments," unpublished.

[22] R. Fantacci and B. Picano, "Edge-based virtual reality over 6G Terahertz channels," *IEEE Netw.*, vol. 35, no. 5, pp. 28–33, Sep./Oct. 2021.

[23] H.-J. Song, H. Hamada, and M. Yaita, "Prototype of KIOSK data downloading system at 300 GHz: Design, technical feasibility, and results," *IEEE Commun. Mag.*, vol. 56, no. 6, pp. 130–136, Jun. 2018.

[24] S. A. Busari, S. Mumtaz, and J. Rodriguez, "Hybrid Precoding techniques for THz massive MIMO in hotspot network deployment," in *Proc. IEEE 91st Veh. Technol. Conf. (VTC-Spring)*, 2020, pp. 1–6.

[25] T. L. Marzetta, E. G. Larsson, H. Yang, and H. Q. Ngo, *Fundamentals of Massive MIMO*. Cambridge, U.K.: Cambridge Univ. Press, 2016.

[26] *5G; Study on Channel Model for Frequencies From 0.5 to 100 GHz, Version 14.0.0*, 3GPP Standard TS 38.901, May 2017. [Online]. Available: https://www.etsi.org/deliver/etsi_tr/138900_138999/138901/14.00.00_60/tr_138901v140000p.pdf

[27] S. Zhang, J. Liu, H. Guo, M. Qi, and N. Kato, "Envisioning device-to-device communications in 6G," *IEEE Netw.*, vol. 34, no. 3, pp. 86–91, May/Jun. 2020.

[28] K.-C. Chen, T. Zhang, R. D. Gitlin, and G. Fettweis, "Ultra-low latency mobile networking," *IEEE Netw.*, vol. 33, no. 2, pp. 181–187, Mar./Apr. 2019.

[29] V. Petrov, T. Kurner, and I. Hosako, "IEEE 802.15.3d: First standardization efforts for sub-terahertz band communications toward 6G," *IEEE Commun. Mag.*, vol. 58, no. 11, pp. 28–33, Nov. 2020.

[30] K. Rikkinen, P. Kyosti, M. E. Leinonen, M. Berg, and A. Parssinen, "THz radio communication: Link budget analysis toward 6G," *IEEE Commun. Mag.*, vol. 58, no. 11, pp. 22–27, Nov. 2020.

[31] C.-L. Cheng and A. Zajić, "Characterization of propagation phenomena relevant for 300 GHz wireless data center links," *IEEE Trans. Antennas Propag.*, vol. 68, no. 2, pp. 1074–1087, Feb. 2020.

[32] X. Su *et al.*, "Multipath and receiver aperture effects in a THz wireless communications link using OAM multiplexing," in *Proc. IEEE Globecom Workshops (GC Wkshps*, 2020, pp. 1–6.

[33] A. Fricke and T. Kürner, "Interference study for THz intra-device communication systems with multiple links," in *Proc. 12th Eur. Conf. Antennas Propag. (EuCAP)*, 2018, pp. 1–5.

[34] J. Fu, P. Juyal, and A. Zajić, "Modeling of 300 GHz chip-to-chip wireless channels in metal enclosures," *IEEE Trans. Wireless Commun.*, vol. 19, no. 5, pp. 3214–3227, May 2020.

[35] B. Yu *et al.*, "Ortho-mode sub-THz interconnect channel for planar chip-to-chip communications," *IEEE Trans. Microw. Theory Techn.*, vol. 66, no. 4, pp. 1864–1873, Apr. 2018.

[36] S. Priebe, C. Jastrow, M. Jacob, T. Kleine-Ostmann, T. Schrader, and T. Kürner, "Channel and propagation measurements at 300 GHz," *IEEE Trans. Antennas Propag.*, vol. 59, no. 5, pp. 1688–1698, May 2011.

[37] S. Priebe, M. Kannicht, M. Jacob, and T. Kürner, "Ultra broadband indoor channel measurements and calibrated ray tracing propagation modeling at THz frequencies," *J. Commun. Netw.*, vol. 15, no. 6, pp. 547–558, 2013.

[38] Y. Xing, T. S. Rappaport, and A. Ghosh, "Millimeter wave and sub-THz indoor radio propagation channel measurements, models, and comparisons in an office environment," *IEEE Commun. Lett.*, vol. 25, no. 10, pp. 3151–3155, Oct. 2021.

[39] S. L. H. Nguyen, J. Järveläinen, A. Karttunen, K. Haneda, and J. Putkonen, "Comparing radio propagation channels between 28 and 140 GHz bands in a shopping mall," in *Proc. Eur. Conf. Antennas Propag. (EuCAP)*, Apr. 2018, pp. 1–5.

[40] S. L. H. Nguyen, K. Haneda, J. Järveläinen, A. Karttunen, and J. Putkonen, "Large-scale parameters of spatio-temporal short-range indoor backhaul channels at 140 GHz," in *Proc. IEEE Veh. Technol. Conf. (VTC)*, Apr. 2021, pp. 1–6.

[41] D. Dupleich, R. Müller, S. Skoblikov, M. Landmann, G. Del Galdo, and R. Thomä, "Characterization of the propagation channel in conference room scenario at 190 GHz," in *Proc. 14th Eur. Conf. Antennas Propag. (EuCAP)*, 2020, pp. 1–5.

[42] L. Pometcu and R. D'Errico, "Large scale and clusters characteristics in indoor sub-THz channels," in *Proc. IEEE 29th Annu. Int. Symp. Pers. Indoor Mobile Radio Commun. (PIMRC)*, 2018, pp. 1405–1409.

[43] A. Schultze, F. Undi, M. Peter, W. Keusgen, and T. Eichler, "Angle-resolved THz channel measurements at 300 GHz in a conference room environment," in *Proc. 34th Gen. Assem. Sci. Symp. Int. Union Radio Sci. (URSI GASS)*, pp. 1–4.

[44] S. Kim and A. Zajić, "Statistical modeling of THz scatter channels," in *Proc. 9th Eur. Conf. Antennas Propagat. (EuCAP)*, 2015, pp. 1–5.

[45] N. Khalid, N. A. Abbasi, and O. B. Akan, "Statistical characterization and analysis of low-THz communication channel for 5G Internet of Things," *Nano Commun. Netw.*, vol. 22, Dec. 2019, Art. no. 100258.

[46] Y. Chen, Y. Li, C. Han, Z. Yu, and G. Wang, "Channel measurement and ray-tracing-statistical hybrid modeling for low-terahertz indoor communications," *IEEE Trans. Wireless Commun.*, vol. 20, no. 12, pp. 8163–8176, Dec. 2021.

[47] S. Ju, Y. Xing, O. Kanhere, and T. S. Rappaport, "Sub-terahertz channel measurements and characterization in a factory building," 2022, *arXiv:2203.03799*.

[48] N. A. Abbasi *et al.*, "Double directional channel measurements for THz communications in an urban environment," 2019, *arXiv:1910.01381*.

[49] N. A. Abbasi *et al.*, "Double directional channel measurements for THz communications in an urban environment," in *Proc. IEEE Int. Conf. Commun. (ICC)*, 2020, pp. 1–6.

[50] Y. Xing and T. S. Rappaport, "Propagation measurements and path loss models for sub-THz in urban microcells," in *Proc. IEEE Int. Conf. Commun.*, 2021, pp. 1–6.

[51] Y. Xing and T. S. Rappaport, "Millimeter wave and terahertz urban microcell propagation measurements and models," *IEEE Commun. Lett.*, vol. 25, no. 12, pp. 3755–3759, Dec. 2021.

[52] S. Ju and T. S. Rappaport, "Sub-terahertz spatial statistical MIMO channel model for urban microcells at 142 GHz," in *Proc. IEEE Global Commun. Conf.*, 2021, pp. 1–6.

[53] F. Undi, A. Schultze, W. Keusgen, M. Peter, and T. Eichler, "Angle-resolved THz channel measurements at 300 GHz in an outdoor environment," in *Proc. IEEE Int. Conf. Commun. Workshops (ICC Workshops)*, 2021, pp. 1–7.

[54] C. Han *et al.*, "Terahertz wireless channels: A holistic survey on measurement, modeling, and analysis," 2021, *arXiv:2111.04522*.

[55] Y. Yang, M. Mandehgar, and D. R. Grischkowsky, "Broadband THz pulse transmission through the atmosphere," *IEEE Trans. THz Sci. Technol.*, vol. 1, no. 1, pp. 264–273, Sep. 2011.

[56] *Attenuation by Atmospheric Gases*, Rec. 676.10, Int. Telecommun. Union, Geneva, Switzerland, Mar. 2013. [Online]. Available: https://www.itu.int/dms_pubrec/itu-r/rec/p/R-REC-P.676-11-201609-I!!PDF-E.pdf

[57] F. Norouzian *et al.*, "Rain attenuation at millimeter wave and low-THz frequencies," *IEEE Trans. Antennas Propag.*, vol. 68, no. 1, pp. 421–431, Jan. 2020.

[58] Y. Amarasinghe, W. Zhang, R. Zhang, D. M. Mittleman, and J. Ma, "Attenuation of terahertz waves by wet snow, dry snow and rain," in *Proc. IEEE Int. Conf. Plasma Sci. (ICOPS)*, 2020, p. 216.

[59] C. Jansen *et al.*, "Diffuse scattering from rough surfaces in THz communication channels," *IEEE Trans. THz Sci. Technol.*, vol. 1, no. 2, pp. 462–472, Nov. 2011.

[60] F. Sheikh, Y. Gao, and T. Kaiser, "A study of diffuse scattering in massive MIMO channels at terahertz frequencies," *IEEE Trans. Antennas Propag.*, vol. 68, no. 2, pp. 997–1008, Feb. 2020.

[61] F. Sheikh, D. Lessy, M. Alissa, and T. Kaiser, "A comparison study of non-specular diffuse scattering models at terahertz frequencies," in *Proc. 1st Int. Workshop Mobile Terahertz Syst. (IWMTS)*, 2018, pp. 1–6.

[62] V. Degli-Esposti, "Indoor environments," in *THz Communications: Paving the Way Towards Wireless Tbps*, T. Kürner, D. Mittelman, and T. Nagatsuma, Eds. Cham, Switzerland: Springer Int., 2022.

[63] K. Du, O. Ozdemir, F. Erden, and I. Guvenc, "Sub-Terahertz and mmWave penetration loss measurements for indoor environments," in *Proc. IEEE Int. Conf. Commun. Workshops (ICC Workshops)*, 2021, pp. 1–6.

[64] R. G. Kouyoumjian and P. H. Pathak, "A uniform geometrical theory of diffraction for an edge in a perfectly conducting surface," *Proc. IEEE*, vol. 62, no. 11, pp. 1448–1461, Nov. 1974.

[65] S. Priebe, M. Jacob, C. Jastrow, T. Kleine-Ostmann, T. Schrader, and T. Kürner, "A comparison of indoor channel measurements and ray tracing simulations at 300 GHz," in *Proc. 35th Int. Conf. Infrared Millimeter Terahertz Waves (IRMMW-THz)*, 2010, pp. 1–2.

[66] G. R. MacCartney, S. Deng, S. Sun, and T. S. Rappaport, "Millimeter-wave human blockage at 73 GHz with a simple double knife-edge diffraction model and extension for directional antennas," in *Proc. IEEE 84th Veh. Technol. Conf. (VTC-Fall)*, 2016, pp. 1–6.

[67] T. Kleine-Ostmann, M. Jacob, S. Priebe, R. Dickhoff, T. Schrader, and T. Kürner, "Diffraction measurements at 60 GHz and 300 GHz for modeling of future THz communication systems," in *Proc. 37th Int. Conf. Infrared Millimeter Terahertz Waves (IRMMW-THz)*, 2012, pp. 1–2.

[68] J. Kokkoniemi, P. Rintanen, J. Lehtomaki, and M. Juntti, "Diffraction effects in Terahertz band—Measurements and analysis," in *Proc. IEEE Global Commun. Conf. (GLOBECOM)*, 2016, pp. 1–6.

[69] W. C. Jakes and D. C. Cox, *Microwave Mobile Communications*. New York, NY, USA: Wiley-IEEE Press, 1994.

[70] J. Högbom, "Aperture synthesis with a non-regular distribution of interferometer baselines," *Astron. Astrophys. Suppl.*, vol. 15, p. 417, Jun. 1974.

[71] *Radio Propagation Measurements and Channel Modeling: Best Practices for Millimeter-Wave and Sub-Terahertz Frequencies*. Cambridge, U.K.: Cambridge Univ. Press, 2022.

[72] A. Papoulis and S. U. Pillai, *Probability, Random Variables and Stochastic Processes*, 4th ed. Boston, MA, USA: McGraw-Hill.

[73] S. Hur, Y.-J. Cho, J. Lee, N.-G. Kang, J. Park, and H. Benn, "Synchronous channel sounder using horn antenna and indoor measurements on 28 GHz," in *Proc. IEEE Int. Black Sea Conf. Commun. Netw. (BlackSeaCom)*, 2014, pp. 83–87.

[74] B. H. Fleury, "An uncertainty relation for WSS processes and its application to WSSUS systems," *IEEE Trans. Commun.*, vol. 44, no. 12, pp. 1632–1634, Dec. 1996.

[75] B. H. Fleury, "First-and second-order characterization of direction dispersion and space selectivity in the radio channel," *IEEE Trans. Inf. Theory*, vol. 46, no. 6, pp. 2027–2044, Sep. 2000.

[76] A. A. M. Saleh and R. Valenzuela, "A statistical model for indoor multipath propagation," *IEEE J. Sel. Areas Commun.*, vol. 5, no. 2, pp. 128–137, Feb. 1987.

[77] S. Aditya, A. F. Molisch, and H. M. Behairy, "A survey on the impact of multipath on wideband time-of-arrival based localization," *Proc. IEEE*, vol. 106, no. 7, pp. 1183–1203, Jul. 2018.

[78] A. F. Molisch, T. Choi, N. Abbasi, F. Rottenberg, and J. Zhang, "Millimeter-wave channels," in *Wiley 5G Ref: Essential 5G Reference Online*. Hoboken, NJ, USA: Wiley, 2021, pp. 1–46.

[79] A. F. Molisch and F. Tufvesson, "Propagation channel models for next-generation wireless communications systems," *IEICE Trans. Commun.*, vol. 97, no. 10, pp. 2022–2034, 2014.

[80] L. Greenstein, V. Erceg, Y. S. Yeh, and M. V. Clark, "A new path-gain/delay-spread propagation model for digital cellular channels," *IEEE Trans. Veh. Technol.*, vol. 46, no. 2, pp. 477–485, May 1997.

JORGE GOMEZ-PONCE (Graduate Student Member, IEEE) received the B.Sc. degree in electronics and telecommunications engineering and the master's degree in telecommunications from the Escuela Superior Politécnica del Litoral, Guayaquil, Ecuador, in 2011 and 2015, respectively, and the M.S.E.E. degree in electrical engineering from the University of Southern California, Los Angeles, CA, USA, in 2019, where he is currently pursuing the Ph.D. degree in electrical engineering.

His current research interests include statistical and ray-tracer modeling for wireless communication channels (e.g., Wi-Fi, UAV, sub-7GHz, mm-wave, and THz), RF systems design and implementation with DSP/FPGA systems, estimation theory and machine learning applied to wireless communications, and cognitive radio systems.

NAVEED A. ABBASI (Member, IEEE) received the bachelor's degree in electrical engineering from Air University, Islamabad, Pakistan, in 2007, the master's degree from Northwestern Polytechnical University, Xi'an, China, in 2010, and the Ph.D. degree from Koc University, Istanbul, Turkey, in 2018.

His current research interests include channel sounder design, measurements and modeling for various wireless communication bands including THz, mm-wave and Wi-fi as well as the applications of machine learning towards wireless communication. He is also interested in molecular and nano-scale communication.

ALAN E. WILLNER (Fellow, IEEE) received the Ph.D. degree from Columbia University, New York, NY, USA, in 1988. He is currently the Steven and Kathryn Sample Chaired Professor of Engineering with the University of Southern California, Los Angeles, CA, USA. He has more than 1400 publications and holds 38 patents. He has received the Presidential Faculty Fellows Award from the White House; IEEE Eric Sumner Technical Field Award; Ellis Island Medal of Honor; Fulbright, Guggenheim, Packard Foundation Fellowships; US DoD Vannevar Bush Faculty Fellowship; IET J. J. Thomson Medal; and OSA Forman Engineering Excellence Award. He is a member of the U.S. National Academy of Engineering, an International Fellow of the U.K. Royal Academy of Engineering, and a Fellow of the National Academy of Inventors, the American Association for the Advancement of Science, the Optical Society of America, and SPIE. His activities include: Co-Chair of US National Academies' Study on Optics & Photonics; the President of OSA and IEEE Photonics Society; and the Editor-in-Chief of *Optics Letters* (OSA), IEEE/OSA JOURNAL OF LIGHTWAVE TECHNOLOGY, and IEEE JOURNAL OF SELECTED TOPICS IN QUANTUM ELECTRONICS.

CHARLIE J. ZHANG (Fellow, IEEE) received the Ph.D. degree from the University of Wisconsin, Madison. He is an SVP and the Head of the Standards and Mobility Innovation Team, Samsung Research America, where he leads research, prototyping, and standards for 5G/6G and future multimedia networks. He is also currently serving as the Chairman of the Board with FiRa Consortium, which is dedicated to the development of seamless user experiences using the secured fine ranging and positioning capabilities of interoperable UWB technologies. From 2009 to 2013, he served as the Vice-Chairman of the 3GPP RAN1 working group and led the development of LTE and LTE-Advanced technologies such as 3D channel modeling, UL-MIMO, CoMP, Carrier Aggregation for TD-LTE.

ANDREAS F. MOLISCH (Fellow, IEEE) received the Dipl.Ing., Ph.D., and Habilitation degrees from the Technical University Vienna, Austria, in 1990, 1994, and 1999, respectively. He spent the next ten years in industry, with FTW, AT&T (Bell) Laboratories, and Mitsubishi Electric Research Labs (where he rose to Chief Wireless Standards Architect). In 2009, he joined the University of Southern California, Los Angeles, CA, USA, as a Professor, and founded the Wireless Devices and Systems Group. In 2017, he was appointed to the Solomon Golomb–Andrew and Erna Viterbi Chair. His research interests revolve around wireless propagation channels, wireless systems design, and their interaction. Recently, his main interests have been wireless channel measurement and modeling for 5G and beyond 5G systems, joint communication-caching-computation, hybrid beamforming, UWB/TOA-based localization, and novel modulation/multiple access methods. Overall, he has published five books (among them the textbook *Wireless Communications*, third edition in 2022), 21 book chapters, 280 journal papers, and 370 conference papers. He is also the inventor of 70 granted (and more than 10 pending) patents, and coauthor of some 70 standards contributions. His work has been cited more than 59 000 times, his H-index is >100, and he is a Clarivate Highly Cited Researcher. He has been an Editor of a number of journals and special issues, General Chair, Technical Program Committee Chair, or Symposium Chair of multiple international conferences, as well as Chairperson of various international standardization groups. He is a Fellow of the National Academy of Inventors, AAAS, and IET, an IEEE Distinguished Lecturer, and a member of the Austrian Academy of Sciences. He has received numerous awards, among them the IET Achievement Medal, the Technical Achievement Awards of IEEE Vehicular Technology Society (Evans Avant-Garde Award) and the IEEE Communications Society (Edwin Howard Armstrong Award), and the Technical Field Award of the IEEE for Communications, the Eric Sumner Award.